Surface Peierls Transition on Cu(001) Covered with Heavier p-Block Metals

Tetsuya Aruga

Department of Chemistry, Graduate School of Science, Kyoto University, Kyoto 606-8502, Japan

Abstract

The Cu(001) surface covered with submonolayer coverages of In and Sn undergoes phase transitions at around 350-400 K. The transition is associated with the surface electronic structure change between low-temperature gapped and high-temperature ungapped ones. The energy gap positions in the k space coincide with the surface Brillouine zone boundaries of the low-temperature phases. These observations imply that the phase transitions are classified into the Peierls-type charge density wave (CDW) phase transition. The CDW ground states are characterized by large overall CDW gaps and long CDW correlation lengths. Structural studies show that the transitions are associated with order–disorder processes. This suggests that these are in strong-coupling regime. However, the associated gapped-ungapped change suggests that the electronic terms play significant role, in contradiction with the strong-coupling scenario. Based on the results of recent works on precise temperature dependence of the CDW gap and critical X-ray scattering, the origin of this dual nature and the detailed mechanism of the phase transition is discussed. It is suggested that the electronic entropy of the CDW ground state is not governed by the overall energy gap but by the gap between the upper band minimum and the Fermi level of the whole system. The dual nature of the surface Peierls transition on Cu(001) originates, on one hand, from the existence at metal surfaces of the two characteristic energy gaps: the overall gap, which determines the CDW stabilization energy, and the upper gap, which governs the electronic entropy. On the other hand, the CDW correlation length is suggested to play another significant role in determining the nature of the Peierls transition. The classification of the Peierls transisions according to the CDW correlation length and the gap size is discussed. It is suggested that the surface Peierls transition on metal-covered Cu(001) covered with heavier p-block metallic elements are qualitatively different from both the weak-coupling CDW transition, with long CDW correlation length and small gaps, and the strong-coupling CDW transitions, with short correlation lengths and large gaps, and should be classified into the third class, which is characterized by long coherence and strong coupling.

Key words: Peierls transition, charge density wave

1 Introduction

The Peierls transition is driven by electron–phonon interaction in metallic materials with the Fermi surfaces of particular, anisotropic topology. Upon cooling down, the normal metal state at high temperatures undergoes a transition to a ground state which is characterized by periodic lattice distortion (PLD) and charge-density waves (CDWs) with the same periodicity. The transition is often called the (Peierls-type) CDW transition. The Peierls transition is, in principle, associated with the changes in transport properties, and hence the technological trends toward electronic devices with nanometer dimensions has been stimulating a growing interest in the Peierls transitions in ultrathin films and wires.

As solid surfaces and interfaces provide quasi-two-dimensional electron systems, efforts have long been paid to find Peierls transitions, which fruited in the last decade in the discovery of intriguing surface phase transitions which were suggested to be the Peierls, or CDW, phase transition [1–4].

The transition on the Ge(111) surface covered with 1/3 monolayers of heavier p-block metallic elements [1] such as Pb and Sn [1,2] has been most intensively studied. (For reviews on this surface from various aspects, see Refs. [5–7].) While the Peierls-like scenario was first suggested and supported by several experimental evidences, an objection was made based on the experiments such as core-level photoemission [8–10], which indicated the order–disorder nature of the phase transition. This contradicts with the displacive mechanism expected in the mean-field theory. It should be noted, however, that one cannot say that the phase transition is not a CDW one only because it is associated with an order–disorder process, since it is well established that the real CDW transitions can be associated with order–disorder processes, in particular, when the electron–phonon coupling is strong [11–14] . Within the framework of the existing theory for the strong-coupling CDW, it is characterized by a large energy gap (larger than 100 meV) and an order–disorder process taking place at a temperature lower than the transition temperature expected by the mean-field theory, which is followed by a gapped–degapped transition at higher temperature. An essential difference between the mean-field, or, weak-coupling CDW senario and the strong-coupling one may be whether or not the intermediate disordered, insulating phase exists. As will be discussed in this article, the detailed mechanism of the transition varies according not only to the electron–phonon coupling strength but also to the CDW correlation length.

Email address: aruga@kuchem.kyoto-u.ac.jp (Tetsuya Aruga).

[1] The heavier p-block metallic elements belong to Group 13–16 in the periodic table of elements and arise from filling of the np subshells.

The phase transitions observed on the other surfaces such as In/Si(111) [3], In/Cu(001) [4,15,16], and Sn/Cu(001) [17] have also been suggested as due to the Peierls mechanism. Among these transitions, those on Cu(001) covered with In and Sn exhibit quite similar characteristics such as ground-state structures commensurate with the substrates, high-temperature Fermi surfaces slightly displaced from the low-temperature surface-Brillouine-zone boundaries, and large energy gaps in the ground states, which are considered as characteristic to strong-coupling CDW phase transitions. On the other hand, these phase transitions are associated with the gapped–degapped transition in the electronic structure, which may indicate weak-coupling nature.

The problems that should be discussed are, firstly, whether or not these transitions can be understood by the existing theories for CDW phase transitions, and secondly, whether there are any specificities of the surface phase transitions as compared with those in bulk materials. In order to address these questions, it is desirable to examine the dynamics of the phase transitions; detailed temperature dependence of the quantities such as the energy gap, diffraction profile, and vibrational spectra would serve as keys.

Most recently, experiments have been carried out along this line on the phase transition at ∼400 K on Cu(001) covered with 0.63-ML In [18,19]. The temperature dependence of the energy gap associated with the CDW formation and the diffraction profile from the CDW phase was precisely measured. The results indicate that the phase transition is composed of two processes which occur successively in a small temperature interval. While the result appears to be qualitatively consistent with the strong-coupling theory at the first glance, the experimental results, the characteristic temperature dependence of the CDW gap in particular, suggest that one has to take into account, firstly, the interplay of the surface resonance band with the electronic system of the substrate, and secondly, the long correlation length of this system, as opposed to the short correlation length supposed in the strong-coupling theory.

In this review article, after the classification of the CDW phase transitions according to the strength of the electron–phonon coupling is briefed in Chapter 2, recent studies on the atomic and electronic structure of a variety of phases and phase transitions on Cu(001) covered with heavier p-block metallic elements are reviewed in Chapter 3. After the mechanism of the phase transitions is discussed based on the recent results in Chapter 4, a general view on the Peierls transition on metals is given in Chapter 5.

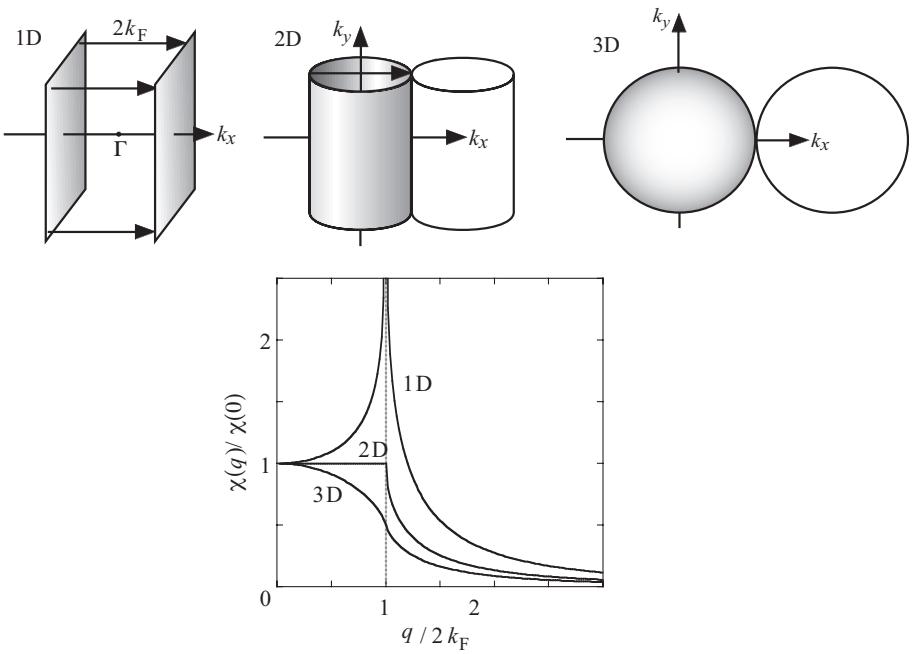

Fig. 1. Fermi surfaces of 1D, 2D and 3D free-electron gases and corresponding Lindhard response functions at $T = 0$.

2 Peierls-type charge-density-wave transition

In this section, the energetics and the mechanism of the Peierls-type CDW phase transition are briefly summarized. For details of the theory and experiments for the bulk materials, see references [20,21]

In the literature, there has often been confusion in terminology regarding CDW states and phase transitions. The term "CDW transition" is used in the literature to imply several different but closely related phenomena. This in turn indicates that the CDW transitions can be classified into several categories, which would help ones avoid the confusion. One of the categories refers to a CDW state possibly stabilized at very low temperatures in low-dimensional free-electron gas *without interacting with the lattice of ions*. The other one postulates the coupling of electrons with the lattice of ion cores, as done by Peierls[22]. Usually the latter one is further classified into subcategories according to the strength of electron–phonon coupling

2.1 Spontaneous charge ordering in free-electron gas

While the Peierls-type CDW state is, as described below, stabilized by electrons and the lattice of ion cores acting each other concertedly, there is a possibility of spontaneous ordering in charge density driven solely by an elec-

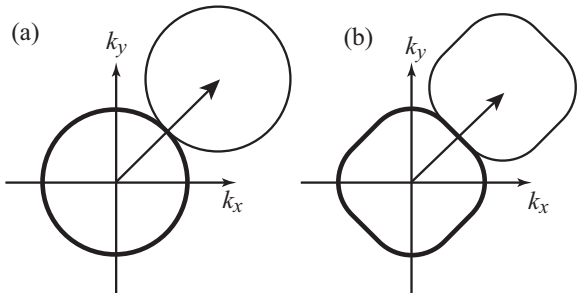

Fig. 2. Two-dimensional Fermi surfaces for (a) "poorly-nested" and (b) "well-nested" cases.

tronic mechanism.

In Fig. 1 is depicted the Lindhard electron response function,

$$\chi(q) = \sum_k \frac{f(E_k) - f(E_{k+q})}{E_k - E_{k+q}}, \tag{1}$$

for free-electron gas at $T = 0$, where $f(E)$ denotes the Fermi distribution function and E_k the electronic energy at wavevector k. Suppose that an electron gas in dimensions $d = 1, 2, 3$ is exposed to a potential $V(q)$. Then the induced charge density in the electron gas can be written as

$$\rho^{\mathrm{ind}}(q) = \chi(q)V(q).$$

For $d = 3$, $\chi(q)$ decreases monotonically with q but the slope diverges at $q = 2k_{\mathrm{F}}$, where k_{F} denotes the Fermi wavevector. For $d = 2$, the singularity is more pronounced. The most pronounced singularity is observed for $d = 1$, where the response function $\chi(q)$ diverges logarithmically at $q = 2k_{\mathrm{F}}$. This suggests that one-dimensional electron gas is unstable and spontaneously forms a charge-ordered state.

In real three-dimensional materials, the Fermi surface is not necessarily a sphere expected for a free-electron gas. $\chi(q)$ for the Fermi surfaces of real materials can have a singularity, or a peak, at $2k_{\mathrm{F}}$ and its magnitude depends on the shape of the Fermi surfaces as schematically shown for a two-dimensional case in Fig. 2. The particular situation where the Fermi surface has a shape that facilitates large $\chi(q = 2k_{\mathrm{F}})$ is called the "Fermi surface nesting."

The charge-ordered states in low-dimensional electron gases are stabilized solely by an electronic mechanism. However, it should be emphasized that this type of charge-ordered states is stable only at very low temperatures, since the singularity at $q = 2k_{\mathrm{F}}$ in $\chi(q)$ is damped steeply with increasing temperature. In other words, electronic condensation energy for such charge-

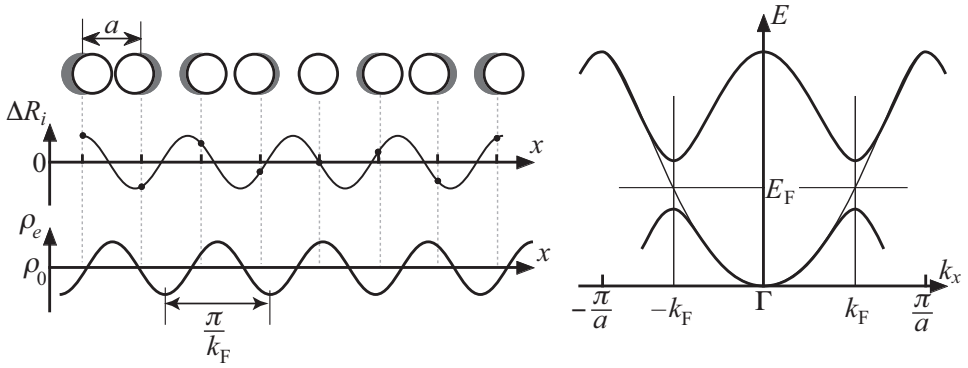

Fig. 3. Schematics of Peierls transition in one dimension. Atomic structure for a longitudinal lattice distortion mode, displacement of i-th atom ΔR_i, electronic charge density $\rho(x)$, and band structure are shown.

ordered states is easily exceeded by electronic entropy at finite temperatures. Realization of charge-density waves at moderate temperatures requires the coupling of electrons with collective modes of ion cores.

2.2 CDW ground states stabilized by electron–phonon coupling

As discussed above, the spontaneous charge redistribution in an electron system is thermally destroyed at moderate temperatures. For the real materials, the electron system is exposed to the periodic potential formed by the lattice of ion cores. While the periodicity of ion cores at equilibrium positions does not necessarily coincide with $\pi/k_{\rm F}$, phonons with a wavevector of $2k_{\rm F}$ can couple with the electron system. This means that phonon spectrum of metals should exhibit anomaly at $q = 2k_{\rm F}$ induced by the singularity of $\chi(q)$ via the screened ion-ion interaction. Actually, a tiny kink is observed at $q = 2k_{\rm F}$ in the phonon dispersion curves $\omega(q)$, which is called the Kohn anomaly [23,24].

For the metals with nested Fermi surfaces, the above effect is much more pronounced, resulting in considerable phonon softening at $q = 2k_{\rm F}$ (giant Kohn anomaly) [25,26]. This leads to a great depression at $q = 2k_{\rm F}$ in the phonon dispersion curve, which sometimes is so drastic that $\omega(2k_{\rm F})$ becomes zero, thus making the phonon mode with $q = 2k_{\rm F}$ be frozen to a static lattice distortion. The phase transition is defined by the temperature at which $\omega(2k_{\rm F}) = 0$. The frozen phonon, or PLD, gives rise to a lattice potential with a period $\pi/k_{\rm F}$, which then produces band gaps at $k = \pm k_{\rm F}$.

Figure 3 shows schematically the PLD, CDW and band structure of the one-dimensional CDW ground state. The stabilization of the CDW state with respect to the metallic state is achieved by the electronic energy lowering near $E_{\rm F}$. Note that, while a longitudinal phonon mode is shown in Fig. 3, transverse phonon modes can also couple with the electron system to yield

transverse lattice distortion [27,28]. For surface systems, it is expected in general that transverse modes are readily coupled with CDW, because vertical displacement of adatoms is not restricted to the vacuum side and is associated with adatom-substrate charge transfer. On the other hand, starting from the CDW ground state, elevating the temperature enhances the electronic excitation across the CDW band gap, which lowers the energetic stability of the CDW state, and eventually the system undergoes a phase transition to the undistorted metallic state.

The enthalpy of the CDW state is lower than that of the metallic phase ($H_{CDW} < H_{metal}$), and the entropy of the metallic phase is larger than that of the CDW phase ($S_{CDW} < S_{metal}$) as there is no band gap across E_{F} in the metallic phase. The free energy ($H - TS$) of the CDW phase is therefore lower than that of the metallic phase at low temperatures, making the CDW state the ground state. Upon elevating temperature, however, the metallic phase tends to have a lower free energy due to the contribution of the entropy term, which is the essential mechanism of the CDW phase transition.

2.3 Classification according to the strength of the electron–phonon coupling

The qualitative description for the CDW transition summarized in the previous subsection is based on the mean-field theory and hence should not be considered to be accurate always. The CDW transitions are usually classified according to the strength of the electron–phonon coupling. At the limit of weak electron–phonon coupling, the CDW band gap, 2Δ, is very small ($\lesssim 100$ meV). This facilitates thermal excitation of electrons across the CDW gap at moderate temperatures. In such a case, the mean-field approximation gives a fairly good description of the transition. In the low-temperature CDW phase, the mean-field theory suggests that the CDW gap varies according to the equation

$$\frac{1}{\lambda} = \int_0^{\epsilon_0} \tanh\left(\frac{\epsilon_k}{2k_{\mathrm{B}}T}\right) \frac{d\epsilon_k}{(\epsilon_k^2 + \Delta^2)^{1/2}}, \tag{2}$$

where ϵ_0 denotes a cutoff energy and λ the dimensionless electron–phonon coupling constant [20]. (The equation is formally the same as that describes the temperature dependence of the superconducting gap within the framework of the BCS theory [29]. The equation for CDW is, however, obtained only within the mean-field approximation and may probably be deviated from the behavior in real materials.) Close to the CDW transition temperature, T_c^{MF}, Eq. (2) can be approximated by

$$\frac{\Delta(T)}{\Delta(0)} = 1.74\left(1 - \frac{T}{T_c^{MF}}\right)^{1/2}. \tag{3}$$

While the direct measurement of the temperature dependence of the gap $\Delta(T)$ for bulk or surface CDW phases has not been done until very recently [18], the temperature dependence of the PLD amplitude coupled to CDW has been measured. Note that the PLD amplitude is proportional to the order parameter $\Delta(T)$ within the mean-field theory. The lattice distortion amplitudes for some bulk compounds appear to be in reasonable agreement with the temperature dependence of Δ as expected from Eq. (2) [20,30], although the experimental temperature dependence is steeper at temperatures close to the transition temperature, which may be explained as due to the effect of critical fluctuation. The distortion amplitudes of PLD in bulk CDW materials, such as $K_{0.3}MoO_3$, $K_2[Pt(CN)_4]Br_{0.3}\cdot 3.2H_2O$ and $(TaSe_4)_2I$, are < 0.1 Å.

The Gibbs free energy for the CDW transition as a function of the order parameter Δ

$$G = \int dV \left(A(\nabla\Delta)^2 + a\Delta^2 + b\Delta^4\right) \tag{4}$$

is schematically shown in Fig. 4. For the weak-coupling case, the mean-field approximation may be valid. This suggests that the first term of Eq. (4), which describes the spatial fluctuation of the order parameter, can be neglected. Therefore the transition scenario for the weak-coupling CDW can be schematized as shown in Fig. 4(a): The free energy G has a single minimum at $\Delta = 0$ in the high-temperature normal-metal state and changes at low temperatures to a double-minima shape, resulting in a broken-symmetry CDW phase. When the temperature approaches the mean-field transition temperature T_c^{MF} from below, the $\Delta(T)$ curve in the CDW phase gradually changes to that for the metallic phase.

Microscopically, the weak-coupling CDW transition is driven predominantly by electronic entropy. At low temperatures, the system is in the CDW ground state, which is stabler than the normal-metal state by an energy proportional to Δ^2. With increasing temperature, the electrons in the lower band are gradually excited across the band gap, which leads to the increase in electronic entropy. At the transition temperature the entropy term for the metallic phase surpasses the energy cost associated with degapping.

For the strong-coupling case, the ground state is also the CDW state which is essentially the same as that in the weak-coupling case. An important difference lies in the magnitude of the energy gap, which is considerably larger than that in the weak-coupling case. This is associated with larger amplitudes of lattice

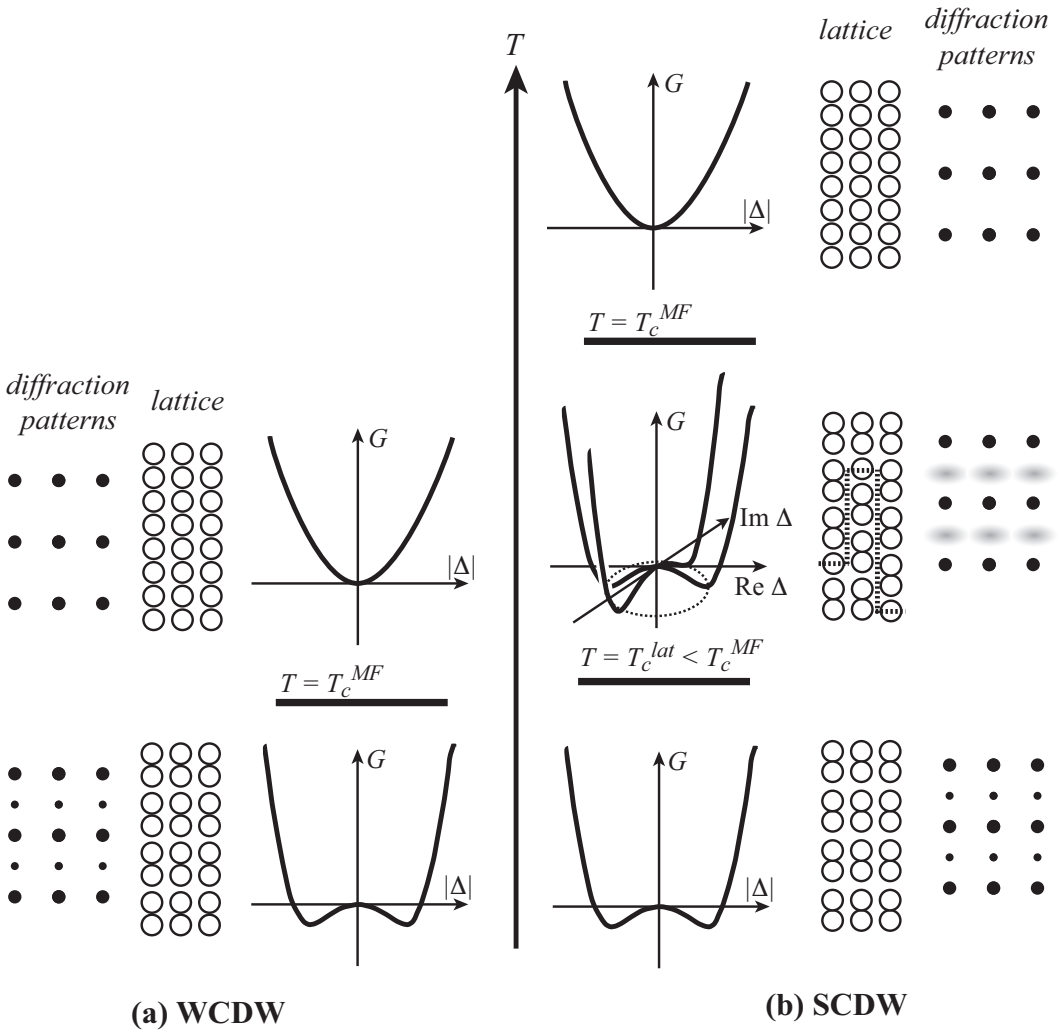

Fig. 4. Temperature-dependent change of Gibbs free energy $G(\Delta)$ for (a) weak–coupling and (b) strong-coupling CDW transitions. Schematic lattice structure and diffraction patterns are also shown. At the weak-coupling limit (a), the ground state has a small lattice distortion amplitude and is transformed to normal-metal state at $T = T_c^{MF}$. For the strong-coupling case, the intermediate phase is formed. This phase has a distorted lattice and short-range CDW, but the spatial phase is fluctuating. The broken lines in the lattice drawing indicate antiphase boundaries. This phase gives rise to diffuse superstructure diffraction spots, which often are too weak and diffuse and hence may be overlooked.

distortion. The high temperature phase is a normal-metal phase the same as that in the weak-coupling case. A consequence of the large $\Delta(0)$ is that the mean-field transition temperature T_c^{MF} is shifted to a very high temperature. For instance, putting the CDW energy gap of $2\Delta(0) = 500$ meV into the mean-field equation for one-dimensional case,

$$2\Delta(0) = 3.52 k_{\mathrm{B}} T_c^{MF}, \tag{5}$$

results in the transition temperature $T_c^{MF} = 1650$ K! In real materials, the lattice degrees of freedom of the CDW phase would not be maintained up to such a high temperature, but the phase fluctuation of the order parameter sets in at $T < T_c^{MF}$. To describe such a phase fluctuation, it is required that the order parameter is expressed as complex. The change of G for the strong-coupling CDW transition as a function of temperature is shown in Fig. 4(b). There is an intermediate phase between the CDW ground state and the normal metal state. In the intermediate phase, the order parameter amplitude $|\Delta|$ is maintained finite and hence the system is insulating. The phase of the order parameter rotates in the bottom of the potential well of $G(\Delta)$, which corresponds in real space to patches of the CDW phase separated by dislocations, or antiphase boundaries. Consequently, the long-range translational order of periodic lattice distortion is destroyed in the intermediate phase. In diffraction experiment, therefore, the superstructure spots associated with the CDW phase are not observed except for diffuse features (blurred spots, streakes, etc.), due to the short-range order, which ara often overlooked. Thus the diffraction spots observed in the intermediate state are apparently the same as those for the normal-metal state.

Within the weak-coupling theory, the electron–phonon coupling is assumed to be independent of q. This, however, is not the case in the strong-coupling regime. An important consequence of the q dependence of the electron–phonon coupling is that the periodicity of CDW tends to be shifted from $2k_{\mathrm{F}}$ or the peak positions of the Lindhard response function which is determined solely by the topology of the Fermi surface. This sometimes results in the CDW periodicity commensurate with the original undistorted lattice. In such a case, the q vector of CDW coincides with the commensurate q position which is preferred by the lattice potential near the peak of the Lindhard response function. This effect should be particularly significant for surface CDWs, because they are subjected to the lattice potential of underlying substrates.

As to the spacial coherence, the weak- and strong-coupling CDW states are usually assumed to have long and short coherence, respectively. The characterization of the CDW ground states and phase transitions will be discussed later in Sections 4 and 5.

Thus the strong-coupling CDW transition consists of two processes, which takes place at $T = T_{cl}$ and T_{ce} ($T_{cl} < T_{ce}$). At $T = T_{cl} < T_c^{MF}$, an order–disorder transition of the lattice takes place, in which the change of the long-range translational symmetry, as observed by diffraction methods, is the same as the weak-coupling CDW transition but the energy gap is maintained. At a very high temperature $T = T_{ce}$, which is usually assumed to be $T_{ce} = T_c^{MF}$, the insulator–metal transition takes place. In materials with very large $\Delta(0)$ (larger than several tenths of eV), the transition at $T = T_{ce}$ is difficult to observe experimentally and hence only the low-temperature transition is

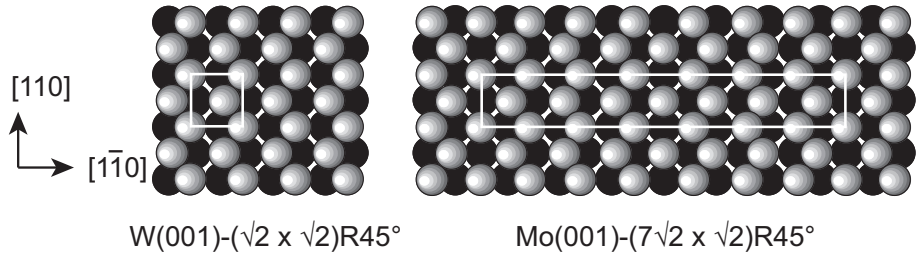

Fig. 5. Models for W(001) and Mo(001) surfaces.

observed. In such cases, the observable "strong-coupling CDW transition" is an order–disorder, insulator–insulator one, and hence is considered to be in contrast with weak-coupling transitions, which are displacive, metal–insulator ones. It is noted that the former is driven by the lattice entropy while the latter by the electronic entropy.

The lack of electronic-structure change during the transition may be a major reason why strong-coupling CDW transitions have not extensively been studied in bulk materials. However, as shown below, it has recently been suggested that surface CDW transitions cannot be categorized simply according to the strength of electron–phonon coupling as in bulk materials. The scenario for the surface CDW transition may be qualitatively different from that in bulk materials.

2.4 Strong-coupling-CDW picture for the phase transitions on W(001) and Mo(001)

The phase transitions on clean W(001) and Mo(001) surfaces were intensively studied for more than two decades since the first observation in 1970's [31–33]. The main focus of interest was placed at whether or not the transition is understood as a surface example of the Peierls-type CDW transition [32–34]. While the studies of these surfaces have been reviewed in several articles [14,35,36], let us briefly describe the characteristics of the phase transition as it is quite instructive within the scope of this article. For further details, see Ref. [14].

The low-temperature structures of W(001) and Mo(001) were determined by many different methods [37–50] and are shown schematically in Fig. 5. The top layer atoms are displaced from ideal (1×1) positions in the $[1\bar{1}0]$ direction to form zig-zag chains. The displacement pattern can be described qualitatively by the frozen-in surface phonon mode $\bar{M}_5$ with $\overrightarrow{q} = (\pi/a)(1, -1)$ for W(001) and $\overrightarrow{q} = (\pi/a)(6/7, -6/7)$ for Mo(001).

Upon heating, the surfaces undergo transition to (1×1) at ∼220 K on W(001) [51] and ∼150 K on Mo(001) [52]. At around 300 K, however, the surface atoms are displaced laterally from ideal (1×1) positions [40,44,51,53–57]. The

surface atoms are disordered at 300 K, giving rise to a (1×1) low-energy electron diffraction (LEED) pattern. It, however, is difficult to verify experimentally whether the surfaces transforms to undisplaced (1×1) structure at higher temperatures. The only experiment up to 600 K by high-energy ion scattering was interpreted to indicate displaced character at 600 K [54], which was later claimed to be consistent with undisplaced structure [58].

Direct observation of the phonon softening at $T > T_c$ was done by means of inelastic He scattering [58–61]. The longitudinal surface phonon mode showed well-defined dispersion at $T > 450$ K, but exhibited considerable softening at $\sim 0.8\bar{M}$ upon approaching T_c, in qualitative agreement with the CDW scenario. Theoretical simulations of vibrational properties were performed [62–66], which succeeded in reproducing the softening. The simulation [65] showed that the probability distribution of the mean square displacement of surface atoms shows a peak at non-zero displacement in the high-temperature phase, which was in accordance with the displaced character of this surface determined experimentally. While the peak was gradually shifted to smaller displacement with increasing temperature, it remained at a non-zero value even at $T = 5T_c$, suggesting that the surface have a disordered character even at ∼1000 K.

Electronic driving mechanism of the phase transition was studied theoretically. Early tight-binding calculation [67,68] already showed that the transition is driven by the instability of d bands with high density of states at E_{F}. The electronic structure calculation of W(001) by linearized augmented plane wave (LAPW) method indicated that a metallic surface resonance band along $\bar{\Gamma}\bar{M}$ for ideal (1×1) surface forms a band gap of ∼1.8 eV at E_{F} when reconstructed to the $(\sqrt{2} \times \sqrt{2})R45°$ structure [69]. The gap extended over $> 60\%$ of $\bar{\Gamma}\bar{M}$, which indicates that the interaction involved is spatially very localized. The CDW correlation length $2\pi/\delta k \lesssim 7$ Å corresponds to only a few unit cell.

The reconstruction on W(001) and Mo(001) are well understood by the local d-state chemical bonding and, at the same time, the atomic structure, the electronic bands, and the phonon dynamics can be consistently described by the theory of strong-coupling CDW phase transition.

3 Phases and transition on Cu(001) covered with heavier p-block metallic elements

3.1 Properties of heavier p-block metallic elements

Surfaces such as Ge(111), Si(111), and Cu(001) covered with monolayers of heavier p-block metallic elements such as In, Tl, Sn, and Pb often exhibit reversible phase transitions with respect to temperature change. These phase transitions have been interpreted as the surface Peierls transition. The present author does not believe that it is merely accidental that the surfaces covered with these elements undergo similar phase transitions. In this subsection, a brief account is given for the properties of these elements.

In bulk solids, some of these heavier p-block metallic elements exhibit crystalline structure which can be considered as distorted from high-symmetry structures such as face-centered and body-centerd cubic. Let me first summarize below the structural properties of these elements.

Among Group 13 elements, metallicity of the elemental solids varies considerably. Boron crystalizes in non-metallic rhombohedral or tetragonal structures. Aluminum is a typical metal forming a face-centered cubic (fcc) structure. Gallium has three crystalline structures, among which α-Ga forms orthorhombic (quasi-tetragonal) structure with $a = 4.519$ Å, $b = 4.526$ Å and $c = 7.657$ Å. Each gallium atom is coordinated by seven neighboring gallium atoms, among which the nearest-neighbor atom is located much closer ($d = 2.48$ Å) than the rests ($d \gtrsim 2.7$ Å) resulting in the Ga_2 dimer structure. This may indicate considerable covalency. Indium crystalizes in body-centered tetragonal structure with $a = 3.253$ Å and $c = 4.946$ Å. This structure can be regarded as distorted fcc. The c/a ratio for indium is 1.520, which is 7.5% larger than the corresponding value for fcc. Due to this distortion, twelve nearest-neighbor atoms in ideal fcc are subgrouped into four nearest neighbors at 3.25 Å and eight next nearest neighbors at 3.38 Å. Thallium crystallizes at room temperature in hexagonal close-packed (hcp) structure with $a = 3.456$ Å and $c = 5.522$ Å. The $c/a = 1.598$ is only 2.1% smaller than the ideal hcp value. The structural characteristics suggest that, among the heavier three elements, the covalency is most significant in the bonding among Ga and the metallicity increases in the series of Ga, In, and Tl.

Group 13 elements have valence electron configuration of ns^2np^1. For aluminum the three valence electrons contribute to metallic bonding. However, for heavier elements, the ns state is shifted to larger binding energies and hence becomes less important in the bonding, which is known as the inert pair effect. The effect is significant in indium and thallium.

Table 1
Electrical resistivity ($\mu\Omega$ cm)

Ga	In	Tl	β-Sn	Pb	As	Sb	Bi	Cu	K
8.20–55.3[a]	8.37	18	11	20	33.3	41.7	120	1.673	7.39

[a] Electrical resistivity of Ga depends on the crystallographic direction.

Among Group 14 elements, the solids of lighter elements, carbon, silicon and germanium, are insulators with larger band gaps for lighter elements; 5.5 eV for diamond, 1.1 eV for Si, and 0.7 eV for Ge. Tin exhibits structural transformation near room temperature. White tin (β-Sn) is stable at room temperature and has a tetragonal lattice, in which each tin atom is coordinated by four nearest neighbors at 3.016 Å and six next nearest neighbors at 3.18 Å. Upon cooling down, it undergoes a transition to gray tin (α-Sn) which has a diamond structure with $a = 6.489$ Å corresponding to nearest neighbor distance of 2.81 Å. While high-temperature β-Sn is metallic, low-temperature α-Sn is a semiconductor with a band gap of 80 meV. Lead, the sixth-row element in Group 14, has a fcc structure with $a = 4.951$ Å and is metallic.

Among Group 15 elements, arsenic, antimony and bismuth crystallize in the same rhombohedral structure. This structure can be considered as puckered sheets of atoms stacked in layers. Each atom has three nearest neighbors and the bond angle is close to 90°. The next-nearest-neighbor distances are 11% (Bi) to 25% (As) larger than the nearest-neighbor distances. The coordination number and the bond angle is consistent with the predominantly covalent bonding between $n\mathrm{p}^3$ hybridized atoms, as $n\mathrm{s}^2$ electrons form inert pairs. The bonding characters results in very small density of states near E_F, making the solid of these elements semimetals.

In Table 1, the electrical resistivity of these elements is compared with that of good metals such as Cu and K. Ga, As, Sb, and Bi exhibit particularly large resistivity. It is also known that the electrical conductivity of these half metals are lower in solid than in liquid. The ratios of conductivity in solid to that in liquid at melting points are ∼0.6 (Ga), 0.67 (Sb), and 0.43 (Bi), which are to be compared with the values of 1.4–1.7 (alkali metals) and ∼2 (Cu, Ag, Au).

It is considered that In, Tl, Sn, and Pb also have a tendency toward localized covalent bonding, while these elements form metallic solids. The covalent character in the bonding suggests strong electron–phonon coupling in the crystals of these elements, which is an important factor in the formation of CDW state as described in the previous section. Actually, in his *"Quantum Theory of Solids"*, R. E. Peierls suggested that the three-dimensional crystalline structure of As, Sb, and Bi can be understood as stabilized by the CDW formation mechanism [22]. On the other hand, strong electron–phonon coupling leads to superconductivity [20]. Heavier p-block elements are known to have relatively high superconducting transition temperature: Ga (1.08 K), In (3.41 K), Tl

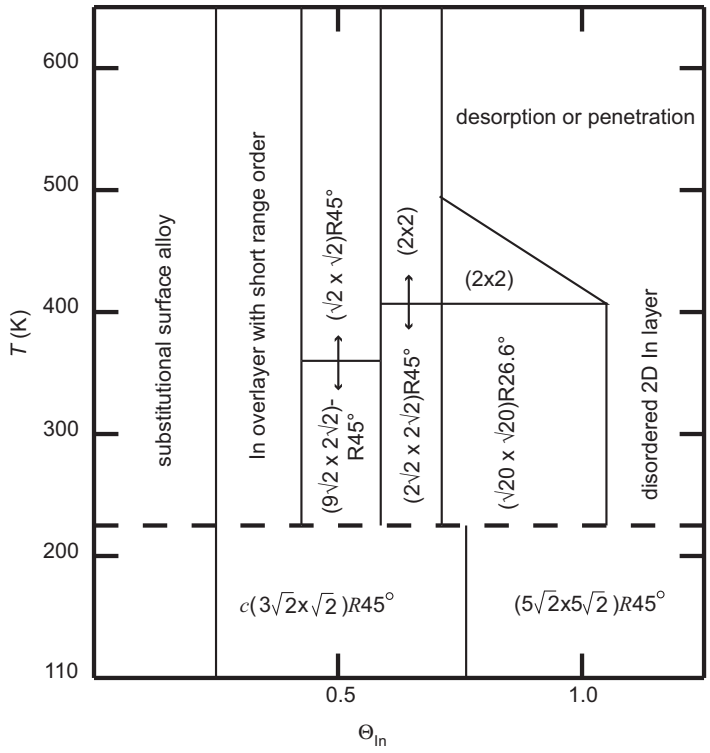

Fig. 6. Phase diagram for In/Cu(001) [70]. The $c(3\sqrt{2} \times \sqrt{2})R45°$ and $(5\sqrt{2}\times 5\sqrt{2})R45°$ phases are metastable and is formed only when In is deposited below 200 K. These phases transform irreversibly to stable phases with corresponding coverages at ∼220 K.

(2.38 K), Sn (3.72 K), and Pb (7.2 K).

All in all, the bonding in heavier p-block elements in Group 13 to 15 can be located between metallic and covalent bonding, resulting in particular characteristics such as distorted crystalline structure and poor electrical conductivity. Note that the degree of covalency varies among these elements: In, Tl, β-Sn, and Pb are relatively closer to the normal metals. It is the monolayers of these four elements that exhibit phase transitions in different surface systems such as In, Tl, and Sn on Cu(001), In on Si(111), and Sn and Pb on Ge(111).

3.2 Structure of heavier p-block metallic element monolayers on Cu(001)

For In/Cu(001), the phases formed upon deposition at room temperature and at $T < 200$K were studied by LEED, scanning tunneling microscopy (STM) and Auger electron spectroscopy (AES) [4,16,70]. The results are summarized in Fig. 6. Upon deposition at room temperature, three ordered phases are

observed: $(9\sqrt{2} \times 2\sqrt{2})R45°$ at $\theta = 0.5$,[2] $(2\sqrt{2} \times 2\sqrt{2})R45°$, or $c(4 \times 4)$, at $\theta = 0.63$, and $(\sqrt{20} \times \sqrt{20})R26.6°$ at $\theta = 0.85$.

Upon heating, the $(9\sqrt{2} \times 2\sqrt{2})R45°$ phase undergoes a phase transition at ∼350 K to $(\sqrt{2} \times \sqrt{2})R45°$, or $c(2 \times 2)$. Similarly, the $(2\sqrt{2} \times 2\sqrt{2})R45°$ and $(\sqrt{20} \times \sqrt{20})R26.6°$ phases are transformed to (2×2) at ∼400 K. These transitions are reversible with respect to temperature change.

The STM image and LEED pattern for the $(9\sqrt{2}\times2\sqrt{2})R45°$ phase is shown in Fig. 7. The surface is composed of parallel stripes of distorted $(\sqrt{2}\times\sqrt{2})R45°$ domains with a width of $\sim 2a_{\sqrt{2}}$, where $a_{\sqrt{2}}$ denotes the lattice constant of $(\sqrt{2}\times\sqrt{2})R45°$. Neighboring $(\sqrt{2}\times\sqrt{2})R45°$ stripes are in anti-phase relation. Between the $(\sqrt{2} \times \sqrt{2})R45°$ stripes, individual atoms are not well resolved but atomic rows running alternatively along [110] and $[1\bar{1}0]$ are observed. Thus the surface is highly anisotropic. The LEED pattern shown in Fig. 7(b) is complicated but is consistent with the $(9\sqrt{2}\times2\sqrt{2})R45°$ structure. While the intensity of each spot depends on the atomic arrangement in the unit cell, the fact that the (1/2 1/2) spot is always missing is consistent with the existence of a glide line along [100]. Fig. 7(c) shows the Fourier transform of the wide-area STM image for the $(9\sqrt{2} \times 2\sqrt{2})R45°$ structure, which is in good agreement with the LEED pattern that is a superposition of the contributions from two equiprobable domains rotated by 90° from each other. It is worthwhile to note that the weak fluctuation in spatial phase is observed. The distorted $(\sqrt{2}\times\sqrt{2})R45°$ stripes are not uniform along [010] but are wandering slightly as seen in the STM image shown in Fig. 7.

On the other hand, the room-temperature structures at higher coverages, $(2\sqrt{2}\times2\sqrt{2})R45°$ and $(\sqrt{20}\times\sqrt{20})R26.6°$, exhibit isotropic STM images with four-fold symmetry as shown in Fig. 8. In the STM image for $(2\sqrt{2}\times2\sqrt{2})R45°$, five protrusions are observed in a unit cell, which agrees with the In coverage of 0.63 determined separately [70]. Structure analyses by LEED [71] and surface X-ray diffraction [72] indicate that an In overlayer with coverage of 5/8 is formed on Cu(001) and that four In atoms out of five per unit cell occupy the site slightly shifted from four-fold hollow sites, while the other In atom occupies a four-fold hollow site. The structure can be understood as a (1×1) structure with a dense array of line vacancies as shown in Fig. 8. (Alternatively, it is also possible to consider this structure as $(\sqrt{2} \times \sqrt{2})R45°$ with interstitial In atoms.) The $(\sqrt{20} \times \sqrt{20})R26.6°$ structure has a complex atomic arrangement, in which all the In atoms are on the (2×2) mesh, as shown by the dotted line in Fig. 8(c). The density of protrusions observed by STM amounts to only 0.6. It was suggested that the second layer is composed of an $In_{1/4}Cu_{3/4}$ alloy with (2×2) periodicity [16].

[2] The In coverage for $(9\sqrt{2} \times 2\sqrt{2})R45°$ was first reported as 1.0, but was later determined to be 0.5 [70].

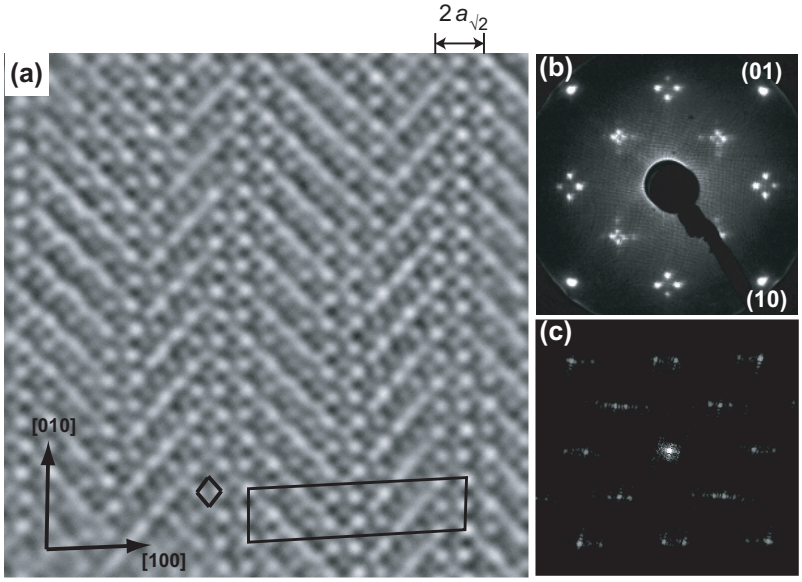

Fig. 7. (a) STM image for the $(9\sqrt{2}\times 2\sqrt{2})R45°$ surface. A small square and a large rectangle indicate the unit cells of (1×1) and $(9\sqrt{2}\times 2\sqrt{2})R45°$, respectively. (b) LEED pattern for the same surface [4]. (c) 2D Fourier transform of the STM image.

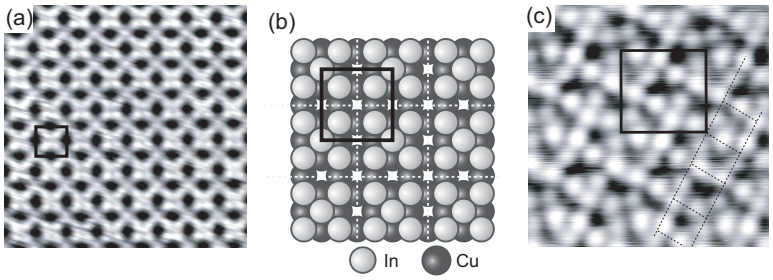

Fig. 8. (a) STM image for the $(2\sqrt{2}\times 2\sqrt{2})R45°$ surface. (b) Line-dislocation model for $(2\sqrt{2}\times 2\sqrt{2})R45°$. Solid lines indicate the unit cell. White broken lines indicate the line vacancies formed in the (1×1) lattice of In. Note that the actual In atom positions are shifted from four-fold hollow sites. (c) STM image for the $(\sqrt{20}\times\sqrt{20})R26.6°$ surface [70]. Solid lines indicate the unit cells. The dotted lines indicate the (2×2) mesh.

The above three surfaces undergo phase transitions upon heating. The translational symmetries of the STM images of the high-temperature phases agree with those observed by LEED. For the transition between $(9\sqrt{2}\times 2\sqrt{2})R45°$ and $(\sqrt{2}\times\sqrt{2})R45°$, the coverage is maintained at 0.5. Since the $(9\sqrt{2}\times 2\sqrt{2})R45°$ structure consists of striped domains of distorted $(\sqrt{2}\times\sqrt{2})R45°$, a displacive mechanism may be probable. Note, however, that the image of $(\sqrt{2}\times\sqrt{2})R45°$ is associated with considerable noise [4] due possibly to the thermal motion of atoms faster than the scanning, which may suggest disordered nature of the high-temperature phase. The STM data does not serve a decisive information to determine the trasition mechanism.

For the phase transition at $\theta_{\rm In} = 0.63$, STM showed that the high-temperature

surface is covered uniformly by the (2×2) structure, which is in agreement with the translational symmetry observed by LEED. However, individual atoms were not resolved but smeared out to give rise to a (2×2) mesh pattern [15]. On the other hand, the coverage determined for the low temperature $(2\sqrt{2} \times 2\sqrt{2})R45°$ phase is 5/8, which is incompatible with the long-range (2×2) symmetry: The number of In atoms per unit cell should be an integer! This indicates that there is a kind of structural disorder in the high temperature phase; the (2×2) symmetry observed by LEED and STM should be temporal average of the fluctuating surface structure. In order to quantitatively analyse the disordered structures, precise experiments are necessary. We will discuss the mechanism of this phase transition in the following section.

For tin adsorption on Cu(001), four ordered structures are formed within submonolayer coverages upon deposition at room temperature [73]. For the first structure, which exhibits a complex LEED pattern, a structure model was proposed which consists of (2×2) patches separated by anti-phase domain boundaries [74]. This is similar to the Cu(001)-$(9\sqrt{2} \times 2\sqrt{2})R45°$-In structure which is understood as distorted $(\sqrt{2} \times \sqrt{2})R45°$ with antiphase line dislocations oriented along [110]. In this case, however, antiphase domain boundaries are assumed to run along [110] as well as along $[1\bar{1}0]$ forming a two-dimensional network. Further deposition results in (6×2), $(3\sqrt{2} \times \sqrt{2})R45°$, and $(2\sqrt{2} \times 2\sqrt{2})R45°$ structures. Among these ordered structures, the $(3\sqrt{2} \times \sqrt{2})R45°$ structure was analysed by dynamical LEED, which yielded a structural model shown in Fig. 9 with a Pendry reliability factor $R_{\mathrm{P}} = 0.26$ [75]. The model corresponds to a nominal Sn coverage of 1/2. With this value as a reference, the coverages for the complex, (6×2), and $(2\sqrt{2}\times2\sqrt{2})R45°$ phases were estimated to be 0.21–0.25, 0.37–0.42, and 0.63–0.7 [73,74]. A study by RBS/channelling indicated the alloying at submonolayer coverages [76].

The structure model for the Cu(001)-$(3\sqrt{2} \times \sqrt{2})R45°$-Sn surface consists of a $Cu_{1/3}Sn_{1/2}$ alloy layer on top of Cu(001). This can be understood that the stripes of $(\sqrt{2} \times \sqrt{2})R45°$-CuSn is separated by line defects, which actually are Cu vacancies running along [010].

Upon annealing, the $(3\sqrt{2} \times \sqrt{2})R45°$ phase undergoes a phase transition at ∼360 K to $(\sqrt{2} \times \sqrt{2})R45°$ [17]. The transition is reversible with respect to temperature change. The structural analysis of the high temperature phase has not yet been reported. The toplayer composition of the low-temperature phase, $Cu_{1/3}Sn_{1/2}$, is not consistent with the apparent translational symmetry of the high-temperature phase. This suggests either (a) that the transition is associated with long-range mass transfer (e.g., of Cu atoms between terraces and steps) or (b) that the high-temperature phase has a disordered structure with the $(\sqrt{2}\times\sqrt{2})R45°$ LEED pattern being temporal and/or spacial average.

For thallium deposition on Cu(001) at room temperature [77–79], the $(2\sqrt{2} \times$

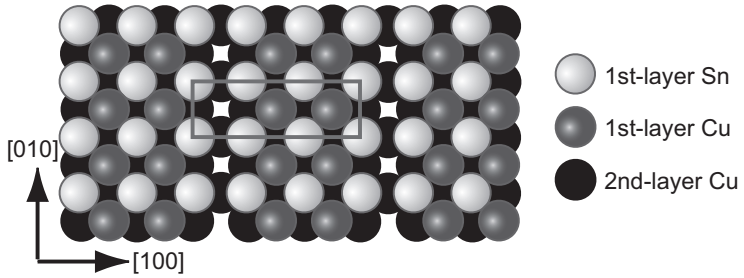

Fig. 9. Top view of the structure model for Cu(001)-$(3\sqrt{2} \times \sqrt{2})R45°$-Sn [75]. Rectangle shows the unit cell.

$2\sqrt{2})R45°$ phase is first formed, whose LEED intensity becomes maximum at $\theta = 0.25$ [3] and disappears over a small range of coverage [79]. While no ordered structures are observed, the AES signal intensity as a function of deposition time shows a kink at $\theta \sim 0.38$ indicating a quick decrease of thallium uptake rate. Further increase of thallium coverage leads to the appearance of another ordered structure, designated as $\begin{pmatrix} 4 & 0 \\ 2 & 7 \end{pmatrix}$ at $\theta \sim 0.52$. This is then followed by a $\begin{pmatrix} 4 & 0 \\ 2 & 6 \end{pmatrix}$ phase at $\theta \sim 0.52$ which is the saturation coverage. It was assumed that the $\begin{pmatrix} 4 & 0 \\ 2 & 6 \end{pmatrix}$ phase is composed of a dense quasi-hexagonal monolayer of thallium atoms with the metallic radius. The coverage for each phase was then estimated based on the AES result. It was assumed that the kink in the uptake curve corresponded to the change in the growth mode from one-dimensional linear-chain to two-dimensional dense-monolayer growth.

In the coverage range between the disappearance of $(2\sqrt{2} \times 2\sqrt{2})R45°$ and the kink in the uptake curve, cooling the surface to 100 K resulted in a set of new LEED patterns each existing over a narrow coverage range [79]. Among the structures, a $(2\sqrt{2} \times 2\sqrt{2})R45°$ phase was assumed to have an undistorted parallel linear-chain structure, and a $(6\sqrt{2} \times 2\sqrt{2})R45°$ phase a more dense, distorted linear-chain structure. Note that structure analysis has not yet been carried out for these phases on Tl/Cu(001) and that no LEED experiments at elevated temperatures has been reported.

The structure of Pb/Cu(001) has also been studied. Lead depostion on Cu(001) at room temperature results in the formation of $(2\sqrt{2} \times 2\sqrt{2})R45°$ at a submonolayer coverage and $c(5\sqrt{2} \times \sqrt{2})R45°$ at the completion of a monolayer

[3] In the original publications [77–79], the coverages are given as ratios to that of a hexagonal-closed-packed thallium monolayer, it is given here as fractions of the number density of a Cu(001) plane.

Table 2
Nearest neighbor distance in elemental solids (Å)

In	Tl	Sn	Pb	Bi	Cu
3.24 (*1.27*)	3.41 (*1.33*)	3.02 (*1.18*)	3.50 (*1.37*)	3.06 (*1.20*)	2.56 (*1.00*)

Figures in parantheses are relative values.

[73,80–84]. The latter structure was assumed to be a quasi-hexagonal close-packed monolayer. Further deposition leads to the growth of three-dimensional islands of lead. No structural transitions were observed by cooling the substrate down to 77 K [80]. The possibility of phase transitions at high temperatures has not yet been examined.

It is also noted that a variety of ordered structures are formed by bismuth adsorption on Cu(001) [85,86], among which the $c(9\sqrt{2} \times \sqrt{2})R45°$ seems to have atomic arrangement similar to that of the $(9\sqrt{2} \times 2\sqrt{2})R45°$ phase on In/Cu(001). Phase transition at high temperatures, however, has not yet been examined.

To summarize, many structures are observed for submonolayer coverages of In, Tl, Sn, Pb, and Bi on Cu(001). Because the size of adsorbate atoms is significantly larger than that of Cu (see Table 2), adsorbate atoms cannot occupy the nearest-neighbor four-fold hollow sites. It is therefore expected that the adsorbate atoms tend to occupy next-nearest-neighbor sites at a distance of $a_{\sqrt{2}} = 3.615$ Å. This should result in a $(\sqrt{2}\times\sqrt{2})R45°$ overlayer in the simplest case. Most of the actual structures indeed have local building blocks similar to $(\sqrt{2} \times \sqrt{2})R45°$, but in a long range they are modulated differently, yielding a variety of periodicities. These structures can be understood by combinations of line dislocations exerted onto the $(\sqrt{2} \times \sqrt{2})R45°$ lattice. For In and Sn on Cu(001), the complex room temperature structures undergo phase transitions upon heating to simple $(\sqrt{2} \times \sqrt{2})R45°$ or (2×2) structures. On the other hand, as far as the present anthor is aware of, no results have been reported for the structural changes upon heating the Tl, Pb and Bi structures on Cu(001).

3.3 Electronic structure and its relevance to the phase transitions

The evolution of the valence electronic structure of In/Cu(001) as a function of In coverage has been studied thoroughly by angle-resolved photoelectron spectroscopy (ARPES) [70,87]. The valence electronic structure of the Cu substrate is composed of d bands, whose maximum is located at ∼2 eV below $E_{\rm F}$, and nearly-free-electron-like sp bands. The In adsorption induces the formation of two-dimensional surface resonance bands with nearly-free-electron-like dispersion.

The overall dispersion of the In-induced surface resonance band is schemati-

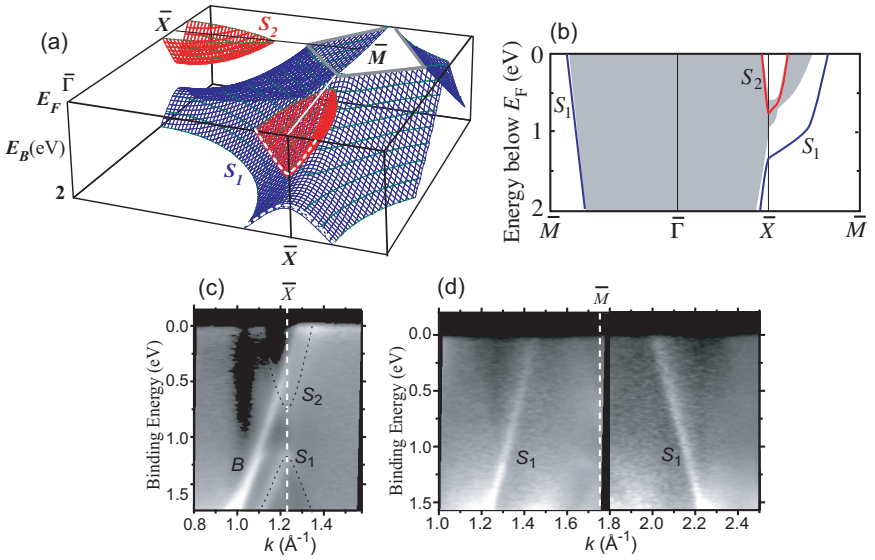

Fig. 10. (a) A schematic of the surface resonance band, for a quadrant of (1×1) surface Brillouine zone, in the high-temperature normal-metal state of In/Cu(001). 2D Fermi surface is shown on the bottom plane. (b) Dispersion of the surface resonance band for the high temperature $(\sqrt{2} \times \sqrt{2})R45°$ phase ($\theta_{\rm In} = 0.5$) along high-symmetry lines. The shaded area indicates the Cu bulk bands projected onto the (001) plane. (c,d) Surface resonance bands mapped at $\theta_{\rm In} = 0.63$ along [110] (c) and [100] (d).

cally shown in Fig. 10 [70,87]. With increasing In coverage, the surface resonance band denoted as S_1 in Fig. 10 is first observed at $\theta_{\rm In} \sim 0.25$ split from the edge of the projected bulk Cu sp band. The S_1 resonance is shifted gradually to lower energies with increasing coverage [70]. The resonance band is nearly parabolic around the $\bar{\Gamma}_{nm}$ points and exhibits hybridization gaps along the (1×1) surface Brillouine zone boundaries. While the upper band S_2 is not very clearly observed in the experiment with photons of $h\nu = 21.22$ eV due to the broadening induced by the coupling with substrate electrons, the experiment with 80-eV photons indicated more clearly the upper band as shown in Fig. 10 (c) [15]. The dispersion along high-symmetry directions are shown in Fig. 10 (b) along with the Cu bulk bands projected onto the (001) plane. Note that the projected bulk bands shown are for the (1×1) symmetry and that most of the projected band gaps disappear on the surface covered with In superstructures, making the In-induced states resonances.

Fermi surface mapping experiments were also done for coverages from 0.5 to 0.85, in which the photoemission intensity was mapped out with the analyzer energy window maintained at $E_{\rm F}$ while scanning the electron energy analyzer in azimuthal and polar angles [15,87]. This showed a nearly circular Fermi surface as shown in Fig. 11(a). The overall shape of the Fermi surface is unchanged with increasing coverage. The radius is increased gradually as the surface resonance band is shifted to lower energies with increasing coverage, but the increase is very small ($\sim 2\%$ between $\theta_{\rm In} = 0.5$ and 0.85). The Fermi

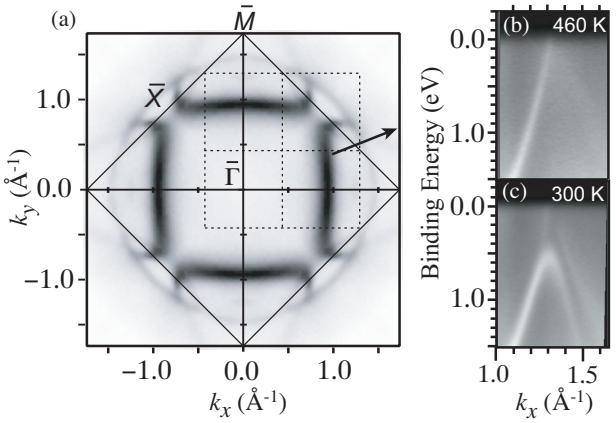

Fig. 11. (a) Fermi surface mapped for Cu(001)-$(2\sqrt{2} \times \sqrt{2})R45°$-In [87]. A circular feature with an approximate radius of 1.4 Å is the Fermi surface constituted by the In-induced surface resonance bands. Strong features inside the circle are due to the bulk Cu bands. The arrow indicates the path along which the band mappings were measured. ARPES band mappings taken at (b) 460 and (c) 300 K for In/Cu(001) of $\theta_{\rm In} = 0.63$ [15].

surface constituted by the In-induced surface resonance band was reproduced by a theoretical calculation, which showed that the surface resonance has a p character [88].

Upon the phase transition from the high- to low-temperature phase, a band gap at $E_{\rm F}$ is formed. The observation was first reported for the phase transition between high-temperature $(\sqrt{2} \times \sqrt{2})R45°$ and low-temperature $(9\sqrt{2} \times 2\sqrt{2})R45°$ at $\theta_{\rm In} = 0.5$ [4], and later for the phase transition between the high-temperature (2×2) and low-temperature $(2\sqrt{2} \times 2\sqrt{2})R45°$ at $\theta_{\rm In} = 0.63$ [15]. Typical ARPES data for the latter case is shown in Fig. 11. The data was obtained at the k space region where the Fermi surface crosses the surface Brillouine zone of the low-temperature $(2\sqrt{2} \times 2\sqrt{2})R45°$ phase. While the band is metallic at high temperatures, it is folded back at a binding energy of ~ 0.6 eV at room temperature, resulting in a band gap at $E_{\rm F}$. The band gap at $E_{\rm F}$ was observed at the k-space region where the $(2\sqrt{2} \times 2\sqrt{2})R45°$ surface Brillouine zone and the high-temperature Fermi surface are separated within $\sim$ 0.1Å. The back-folding points in the k space are aligned on the surface Brillouine zone of $(2\sqrt{2} \times 2\sqrt{2})R45°$, indicating that the band gap formation is due to the lattice potential of the low-temperature superstructure.

At the k region where the Fermi surface is located by > 0.1 Å away from the $(2\sqrt{2} \times 2\sqrt{2})R45°$-In Brillouine zone boudary (for example, along the $\bar{\Gamma}$-$\bar{M}$ direction), no gap is formed at $E_{\rm F}$ but a very small (< 0.1 eV) band gap is formed *below* $E_{\rm F}$ on the surface Brillouine zone boundary. Since the k dependence of the gap size $\Delta(k)$ is determined by the real-space lattice potential $U(r)$ associated with the periodic lattice distortion, the above result

may be rephrased that the atomic arrangement in the low-temperature phase takes place so that the energy gain associated with the gap formation at E_{F} is maximized.

A very similar observation was reported for the phase transition between $(3\sqrt{2} \times \sqrt{2})R45^\circ$ and $(\sqrt{2} \times \sqrt{2})R45^\circ$ on Sn/Cu(001) [17]. The Fermi surface for the high-temperature $(\sqrt{2} \times \sqrt{2})R45^\circ$-Sn phase has a circular shape as those of In/Cu(001) with similar size: The Fermi wavevector along $\bar{\Gamma} - \bar{M}$ for $(\sqrt{2} \times \sqrt{2})R45^\circ$-Sn is $k_{\mathrm{F}} = 1.46$ Å^{-1}, while that for In/Cu(001) changes from 1.42 Å^{-1} at $\theta_{\mathrm{In}} = 0.5$ to 1.45 Å^{-1} at $\theta_{\mathrm{In}} = 0.63$ and remains unchanged upon further increase of the In coverage up to 0.85. The Fermi surfaces on In/Cu(001) and Sn/Cu(001) have very similar shape and size, which may be surprising considering that the numbers of valence electrons of In and Sn are different. As in the cases of In/Cu(001), the phase transition on Sn/Cu(001) is also associated with the formation and disappearance of an electronic energy gap across E_{F} along the surface Brillouine zone boundary of the low temperature phase. The size of the energy gap was comparable to those for In/Cu(001). The Fermi surface nesting in this case is also imperfect: The CDW energy gap was observed at k within 0.04 Å^{-1} from the surface Brillouine zone boundary of the low-temperature $(3\sqrt{2} \times \sqrt{2})R45^\circ$ structure.

These observations indicate that the low-temperature phases have lower electronic energies and lower electronic entropies than those of the corresponding high-temperature phases. While the band gap is formed only partially, its magnitude is large enough to acount for the transition temperatures of 350–400 K (see Eq. (5)) and thus the low-temperature structures are understood as the Peierls-type CDW phases stabilized by the Fermi surface nesting and electron–phonon coupling.

Different parts of the Fermi surfaces are responsible for the gap opening in each superstructure. In all cases, the resultant CDW phases are commensurate with the substrate lattice and large (~ 1 eV) band gaps are formed at k positions slightly deviated from k_{F} in the high temperature phases. These characteristics are in accordance with the strong electron–phonon coupling and its strong q dependence. The mechanism that yields much different superstructures from similar Fermi surfaces should involve firstly the strong q dependence of the electron–phonon coupling. In and Sn are metallic but have tendencies toward covalent and directional bonding, which would result in different structures depending on small differences in coverage, k_{F}, and so on.

The second factor that may govern the formation of different superstructures from very similar Fermi surfaces is the contribution of the bulk electronic states. In a surface system like In/Cu(001), a semi-infinite metallic substrate is in contact with an overlayer and hence the bulk electronic system is, in principle, affected by the lattice potential formed by the surface super-

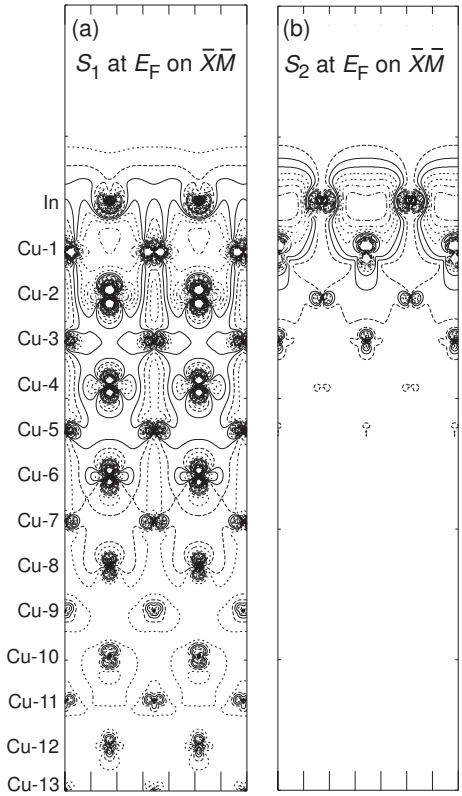

Fig. 12. Wavefunctions for the (a) S_1 and (b) S_2 surface resonance band at the k points where the band crosses E_F along $\bar{X}\bar{M}$.

structure. For instance, this effect seems to be significant in the formation of $(9\sqrt{2} \times 2\sqrt{2})R45°$ superstructure, for which the nesting condition is not simple. The $9\sqrt{2}$ period is not associated with $2k_F$ but corresponds to $\frac{2}{3}k_F$. In an isolated one-dimensional system with only one conduction band, the nesting condition is simply expressed as $q_{\|} = 2k_F$ [89]. On the other hand, in surface systems, substrate metallic bands coexist with the surface one that undergoes the nesting. In such a multi-band system, the ground state may differ from the one characterized by $q_{\|} = 2k_F$. The relative stability of the states with different $q_{\|n}$ ($q_{\|n} = \frac{2}{n}k_F$) depends on the gap size and density of states of the substrate bands at $k_{\|} = q_{\|n}$ and $E = E_F$. It is speculated that the nesting at a fraction of $2k_F$ is due to the energetic contribution of the substrate electronic system.

Based on the fact that the Fermi surface constituted by the adsorbate-induced surface resonance band is insensitive to the difference between In and Sn, Martínez-Blanco et al. [17] suggested that the substrate plays a main role and noted "that the Cu(100) surface is prone to an instability, which is triggered by an adsorbate layer." This idea is interesting. Besides the similarity between In- and Sn-covered Cu(001) surfaces, the change of Fermi surface with increasing In coverage on Cu(001) does not correspond to the increase of the number of electrons per unit cell. The surface resonance band, denoted above as S_1,

should not be considered as the band formed by In atomic orbitals. In order to examine this hypothesis, we studied the surface electronic structure of the In/Cu(001) surface by first-principles electronic structure calculation based on the "augmented plane wave + local orbitals (APW+lo)" method [90]. The surface was modeled by a 25-layer Cu(001) slab with $(\sqrt{2} \times \sqrt{2})R45°$-In layers on both sides. The bands corresponding to S_1 and S_2 were reproduced. Remarkably, the wavefunction of the S_1 band is not localized near the surface but is spread over the entire slab. In Fig. 12(a), the wave function of the S_1 band at the k point where the band crosses the Fermi level along $\bar{X}\bar{M}$ is shown. Since we have two In-covered surfaces on both sides of the slab, the S_1 states on both sides, Ψ_a and Ψ_b, interact with each other and form bonding ($\sim \Psi_a + \Psi_b$) and anti-bonding ($\sim \Psi_a - \Psi_b$) states. In Fig. 12(a) is shown wavefunction of the anti-bonding state, which has a nodal plane at the center of the slab (corresponding to the Cu-13 layer) and hence the amplitude near the central plane is overdamped as compared with the real substrate that is much thicker. We therefore understand that the S_1 state penetrates into at least 10-20 layer depth. In contrast, the wavefunction of the S_2 band at the k point where it crosses $E_{\rm F}$ shows strong localization at the surface as shown in Fig. 12(b). This is because this state lies in the projected bulk band gap. The photoemission intensity of the S_1 band is maximum at the completion of an In monolayer [70], which is in agreement with that the S_1 state is not originating from the overlayer but is induced by the adsorption in the Cu(001) substrate at and below the interface.

Some readers may inquire how the difference in the number of electrons for In and Sn should then manifest itself in the electronic structure. Because the system is metallic, valence electrons of In or Sn are well merged into the continuum valence band of the substrate and hence cannot be distinguished. It is only those surface resonance bands split from the edge of the projected bulk band, as mentioned above, that have a relatively high amplitude at the surface. Note that, for semiconductors, such as Si, Ge and GaAs, and insulators such as metal oxides, it is possible to assume that discrete building blocks (a single atom for Si, a pair of Na and Cl atoms for NaCl for instance) are formally associated with definite numbers of electrons, and hence the electron counting rule can be formulated for surface systems [91–93]. For metals, however, electrons are mostly delocalized over the real as well as reciprocal space and hence one cannot argue, for instance, that a $(\sqrt{2} \times \sqrt{2})$-In layer is associated with how many valence electrons.

Note that, since the electronic band involved in the gapped–degapped transition seems to be delocalized into deep bulk, it is possible to assume that the underlying substrate lattice also undergoes structural transition between distorted and undistorted structures, which however has not yet been demonstrated. The existing diffraction studies on In- and Sn-covered Cu(001) do not show such instability in the substrate lattice. To determine the presumably

small displacements of the substrate atoms based on diffraction data that is largely dominated by the surface atoms would require exceptionally careful experiment and analysis.

4 Mechanism of the phase transitions on Cu(001) covered with heavier p-block metallic elements

In the previous subsection, the change of the atomic and electronic structure during the phase transitions was summarized for In- and Sn-covered Cu(001). The phase transitions appear to take place at 350–400 K. The high-temperature phase in each phase transition is characterized by high translational symmetry and metallic surface resonance band, and the low-temperature phase by reduced symmetry and partial energy gap formation at E_{F} along the surface Brillouine zone boundary of the low-temperature phase. The changes are observed in a small temperature interval: The energy gap is not observed slightly above the temperature at which the superstructure LEED spots from the low-temperature structure disappears. According to the conventional picture for the CDW transitions as summarized in Fig. 4, the phase transitions may be interpreted as the weak-coupling CDW transition. On the other hand, the large energy gaps ($\sim$1 eV), partial nesting, and commensurate structures in the low-temperature phases imply that the phase transitions are of strong-coupling nature.

This apparent contradiction was first pointed out for In/Cu(001) in Ref. [15] and later discussed also for Sn/Cu(001) [17]. In order to reveal the driving mechanism of the surface phase transitions, it was desirable to study the critical behavior. For weak-coupling CDW that can be described by the mean-field theory, the energy gap size and the lattice distortion amplitude are proportonal to each other and hence serve as a unique order parameter of the phase transition. On the other hand, according to the conventional strong-coupling CDW scenario, the structural change occurs in two steps: At a low temperature, an *order–disorder* process takes place with the periodic lattice distortion associated with CDW maintained locally, and at a higher temperature a *displacive* change associated with a gapped–degapped transition takes place. Thus it is very important to study the precise temperature dependence of *both atomic and electronic structure* during the phase transition. In this section, the results of such studies for the phase transition on In/Cu(001) at $\theta_{\mathrm{In}} = 0.63$ [18,19] are summarized and the mechanism of the phase transition is discussed.

Precise temperature dependence of the CDW energy gap during the phase transition is important because it serves as an order parameter for the weak-coupling transition. It, however, is usually difficult to determine the *absolute* energy gap experimentally [3,17,94–98], because photoemission is sensitive only to occupied electronic states and angle-resolved inverse photoemission lacks energy resolution sufficient for the precise determination of energy gaps. The CDW ground states in the surface systems have superstructures commensurate to the substrate lattice. Hence the lattice modulation wavevector does not necessarily agree with $2k_{\mathrm{F}}$ but are deviated slightly. It is sometimes assumed that the energy difference between the lower band maximum and E_{F} serves as an order parameter. This, however, is not justified in the commensurate CDW cases, in which the reference energy at which the upper and the lower bands encounter with each other at $T = T_c$ does not agree with E_{F}.

For the $(2\sqrt{2} \times 2\sqrt{2})R45° - (2 \times 2)$ transition on In/Cu(001), both the lower-band minimum and the upper-band maximum were observed directly by ARPES. The experimental geometry is shown in Fig. 13 (a). For the high-temperature (2×2) surface, the Fermi surface crosses the $(2\sqrt{2} \times 2\sqrt{2})R45°$ surface Brillouine zone boundary at $k_y \sim 0.6$ Å^{-1}. Hence, at k_y slightly smaller than 0.6 Å^{-1}, the energy gap will open with respect to the reference energy, δE, lower than E_{F} as shown in Fig. 13 (b). The upper band minimum will then come down below E_{F} at temperatures close enough to T_c.

Figure 13(c) shows the ARPES data taken along k_x at $k_y = 0.51$ Å^{-1} with increasing temperature [18]. At $T = 305$ K, only the lower band is observed, which is folded back at 0.59 eV below E_{F}. The k_x point at which the band is folded back coincides with the $(2\sqrt{2} \times 2\sqrt{2})R45°$ surface Brillouine zone boundary. At $T = 374$ K, the lower-band maximum is shifted to ∼0.50 eV below E_{F} and another feature is observed near E_{F}. Note that the photoemission intensity is normalized to the Fermi distribution function convoluted with the instrumental resolution function. This enables one to recognize features up to ∼0.2 eV above E_{F}. Note that spectra obtained with photon sources of poor spectral purity, such as a He I resonance lamp containing both I_α and I_β lines and synchrotron radiation containing higher-order lines, are sometimes associated with a spurious features above E_{F} when normalized to the Fermi distribution function. However, since a He discharge lamp in combination with a toroidal mirror monochromator was used in this experiment, the observed feature is ascribed to the intrinsic electronic states above E_{F}. At 460 K, at which LEED shows only (2×2) diffraction spots, the two bands are merged into a single metallic band.

The ARPES spectra were measured between $T = 120$ and 410 K. The spectra

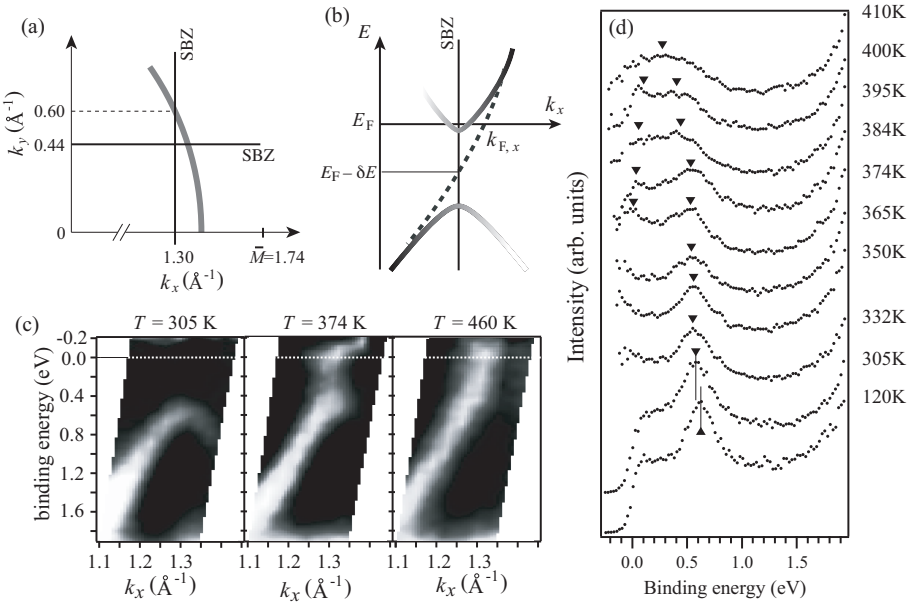

Fig. 13. (a) Relation between 2D Fermi surface for high-temperature (2×2)-In and surface Brillouine zone for $(2\sqrt{2} \times 2\sqrt{2})R45°$-In on Cu(001). (b) Schamatic band structure at $k_y < 0.60$ Å^{-1}. The metallic band (broken line) crosses the surface Brillouine zone boundary at δE below E_F. The CDW gap is opened with respect to this energy, which enables one to observe the upper band minimum by photoemission. (c) Surface resonance band maps measured along $k_y = 0.51$ Å^{-1} at $T = 305$, 374 and 460 K [18]. (d) ARPES spectra at the backfolding point during the phase transition. The spectra except for the bottom two are normalized to the Fermi distribution function.

at $k_x = 1.30$ Å^{-1}, corresponding to the backfolding point, are shown in Fig. 13(d). The tick marks indicate the peak positions determined by fitting two components to each spectrum. The lower-band maximum shows a shift over the entire temperature range measured. The shift by 50 meV between 120 and 305 K is in agreement with the other experiment carried out for this surface by using a different sample and a different instrument [15]. Above 300 K, the shift becomes more and more pronounced. Although the upper band is observed only above ∼370 K, one can determine that the upper-band minimum and the lower-band maximum encounter with each other at ∼300 meV below E_F at ∼410 K to be merged into a single metallic band.

The positions of the lower-band maximum and the upper-band minimum are plotted as a function of temperature in Fig. 14. As far as the present author is aware of, direct observation of the gap temperature dependence for CDW transitions has not been reported. Hence it would be interesting to compare the data with the temperature dependence of the order parameter predicted by the mean-field theory. The solid curves in Fig. 14 shows the temperature dependence of the weak-coupling order parameter as described by Eq. (2). The binding energy at lower-band maximum was fitted with $\delta E + \Delta_l(T)$ and the

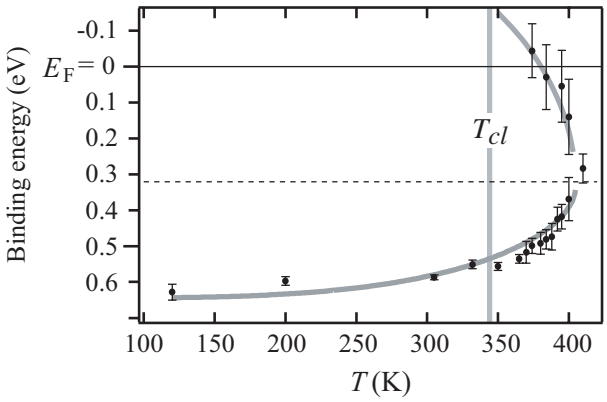

Fig. 14. Temperature dependence of the lower-band maximum and the upper-band minimum for the CDW energy gap for the $(2\sqrt{2} \times 2\sqrt{2})R45° - (2 \times 2)$ phase transition [18]. T_{cl} indicates the transition temperature for the lattice order–disorder transition.

upper-band minimum with $\delta E - \Delta_u(T)$. Δ_l and Δ_u were assumed to behave according to Eq. (2) with different limiting values, $\Delta_l(0)$ and $\Delta_u(0)$, respectively. While there is some discrepancy at 350–380 K, the curves are seemingly in reasonable agreement with the experimental data. The zero-temperature gap is estimated to be $\Delta_l(0) + \Delta_u(0) = 860 \pm 180$ meV.

Temperature dependence of the energy gap was also measured for Sn/Cu(001) [17]. In this case, however, the upper band was not observed, possibly because of the existence of the metallic band at E_F from the perpendicularly-oriented domains. The binding energy of the lower-band maximum was studied as a function of temperature, which showed a steep decrease near T_c. It is not clear at the moment if the band gap also shows the steep decrease. As the high-temperature Fermi surface is a little outside of the $(3\sqrt{2} \times \sqrt{2})R45°$ Brilloune zone boundary, the reference energy, δE, should be located below E_F, which suggests that the decrease of the band gap may be more moderate.

The electronic system on In/Cu(001) show apparently weak-coupling-CDW-like behavior. This may indicate that a process which is governed by electronic system takes place at $T_{ce} = 405$ K. However, it is not evident whether or not the process that should be described by the weak-coupling theory takes place on this surface. Before discussing further, let us study the behavior of the lattice system.

4.2 Critical behavior of the lattice

The result shown in the above subsection shows how the electrons behave during the phase transition. We then have to examine quantitatively how the lattice structure changes in the same temperature range. Hatta et al. measured

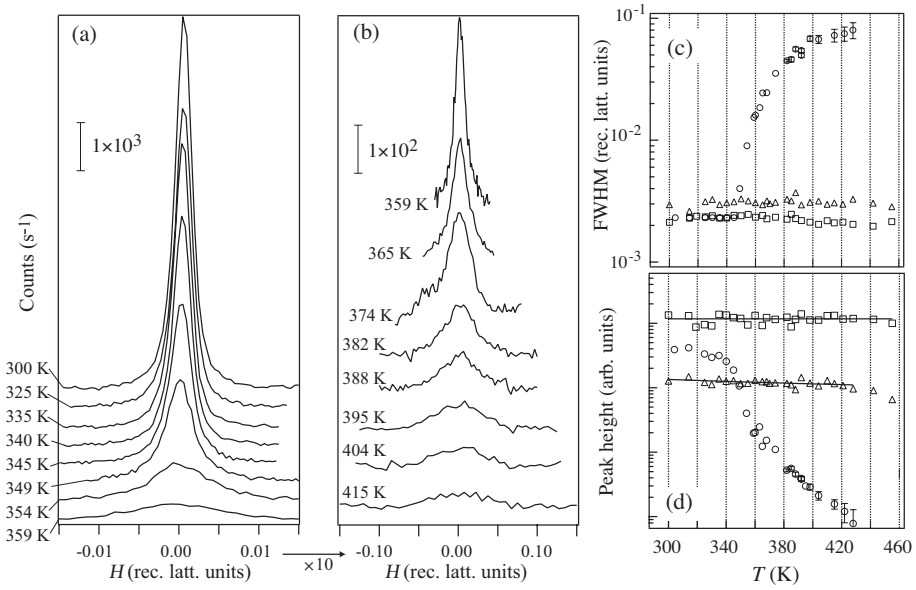

Fig. 15. (a,b) Profile of a quarter-order spot, corresponding to (0 3/2 0.3) in X-ray diffraction notation [19]. (c) Temperature dependence of full width at half maximum for interger- (□), half- (△) and quarter-order (◯) spots. (d) Temperature dependence of peak height.

the critical scattering of X-rays from In/Cu(001) with $\theta_{\rm In} = 0.63$ near the phase transition [19] by using an ultrahigh vacuum X-ray diffractometer at BL13XU of SPring-8 [99]. The use of X-ray diffraction is essential in the measurement of critical scattering because it has the ultrahigh k resolution that is necessary to reveal the behavior close to the critical point, and because it is free from multiple diffraction, which may affect the diffraction profile of LEED.

The X-ray diffraction for integer-, half- and quarter-order spots at constant reciprocal lattice vector perpendicular to the surface were measured at a close temperature interval between 300 and 460 K. The diffraction profiles below ∼340 K were very sharp (full width at half maxima$< 6 \times 10^{-4}$Å^{-1}), which corresponded to the transfer width of ∼1600 Å. This is an order of magnitude larger than achievable in usual LEED experiments and is essential to observe the behavior close to the transition temperature. Note also that the low-temperature width was in agreement with the estimated instrumental resolution limited by the X-ray slit width, suggesting that the natural correlation length was even larger.

Figure 15 shows the diffraction profile of quarter-order spot. While the width does not change up to ∼340 K, it gradually increases above ∼350 K. Along with the broadening, the peak intensity decreases with increasing coverage. The changes of the width and peak intensity are shown in Fig. 15(c) and (d), which also show that interger- and half-order spots exhibit no anomaly up to 460 K.

The profile $S(q,T)$ consists of the Bragg diffraction due to the long-range order and the diffuse scattering due to the critical fluctuation as

$$S(q,T) = I_{long}(T)F(q) + F_{SRO}(q,T) + I_{bg}, \tag{6}$$

where $I_{long}(T)$ denotes the Bragg diffraction, $F(q)$ the instrumental resolution function, F_{SRO} the profile due to the critical scattering convoluted with $F(q)$, and I_{bg} the uniform background. By analyzing the profile at low temperatures, the shape of $F(q)$ was found to be approximated well by a Lorentzian with a constant width. The shape of F_{SRO} was assumed to have also a Lorentzian form

$$F_{SRO}(q,T) = \frac{\chi(T)}{1 + 4q^2\xi_l^2(T)}, \tag{7}$$

where χ denotes the "susceptibility", in analogy to the magnetic susceptibility, $1/\xi_l$ the full width at half maximum of the Lorentzian, and ξ_l the lattice correlation length of the short-range order. Equation (6) was fitted to the measured profile for the quarter-order spot, which resulted in a set of $I_{long}(T)$, $\chi(T)$, and $\xi_l(T)$. In the vicinity of the transition temperature, these three parameters are scaled to powers of the reduced temperature $t = (T - T_{cl})/T_{cl}$, where T_{cl} denotes the transition temperature of the lattice, as $I_{long} \propto (-t)^{2\beta}$, $\chi \propto t^{-\gamma}$ and $\xi_l \propto t^{-\nu}$. The critical exponents, β, γ, and ν, are determined by the universal nature of the phase transition irrespective of the microscopic mechanism.

Figure 16 shows the temperature dependence of the deduced parameters.[4] The fitting of the power functions resulted in $T_{cl} = 345$ K and the critical exponents, $\beta = 0.15 \pm 0.19$, $\gamma = 1.36 \pm 0.62$ and $\nu = 1.14 \pm 0.27$, which are in agreement with those theoretically expected for the two-dimensional Ising universality class: $\beta = 1/8$, $\gamma = 7/4$ and $\nu = 1$. In Fig. 16, the solid lines are shown for these theoretical values. In Fig. 16(c), $1/\xi_l$ is also plotted, which increases linearly with increasing t. It is evident that the data cannot be fitted with the mean-field model, which predicts $\beta = 1/2$, $\gamma = 1$ and $\nu = 1/2$.

The two-dimensional Ising model corresponds to the systems that are described by two-dimensional lattice with its lattice points occupied by either of up ($\sigma_i = 1$) or down ($\sigma_i = -1$) spins. A Hamiltonian of the form

$$H = -\sum_{i,j} J_{ij}\sigma_i\sigma_j$$

describes the interaction energy and is often simplified by setting $J_{ij} = 0$ except for $J_{ij} = J$ for nearest-neighbor pairs. At low enough temperatures the "spins" have a long-range order which may be ferromagnetic, antiferromagnetic, etc. depending on the signs and relative magnitudes of the interac-

[4] In ref.[19], the values of ξ_l ($1/\xi_l$) were scaled larger (smaller) by a factor of $\sqrt{2}$ ($1/\sqrt{2}$).

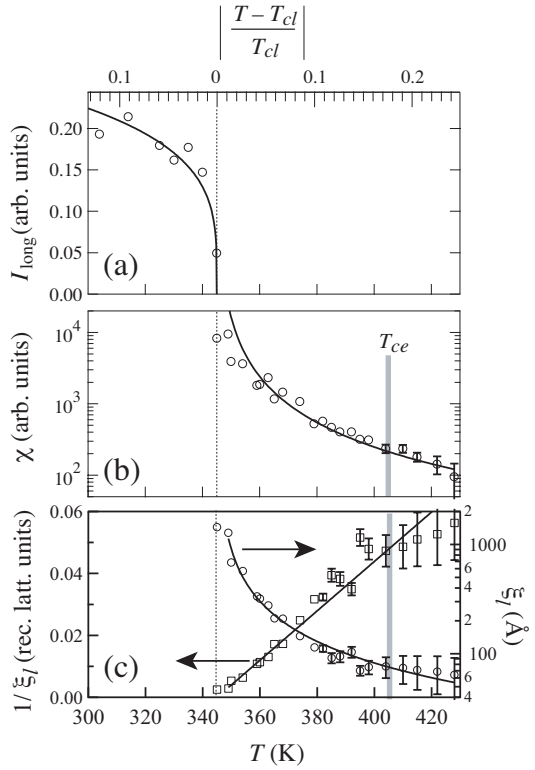

Fig. 16. Temperature dependence of long-range order parameter I_{long}, susceptibility χ, and correlation length ξ_l [19]. Solid curves show $I_{long} \propto |t|^{1/4}$, $\chi \propto t^{-7/4}$, $1/\xi_l \propto t$, and $\xi_l \propto t^{-1}$, where $t = (T - T_{cl})/T_{cl}$.

tions J_{ij}. At a finite temperature, the two-dimensional Ising model exhibits an order–disorder transition, for which the critical exponents above are determined. Approaching the transition temperature from below, the system behaves as follows: At low enough temperature, the long-range order is developed well and the lattice correlation length is, ideally, infinite. Upon approaching T_{cl}, isolated defects are thermally generated which causes the decrease of the long-range-order intensity (I_{long}) below T_{cl}. At $T = T_{cl}$, phase defects are generated and the system is divided into patches in antiphase relation with each other, which destroys the long-range order. With further increasing temperature, the density of phase defects, or antiphase boundaries, increases. The size of the patches is statistically distributed, and the average distance between the antiphase boundaries determines the lattice correlation length. The critical exponent $\nu = 1$ for the two-dimensional Ising class may suggest that the density of antiphase boundaries increases in proportion to the temperature rise.

While the correspondence of the actual atomic structure to the two-dimensional Ising model is not so straightforward as for the transition between $c(4\times2)$ and (2×1) on Si(001) [100–102], it is possible to map the $(2\sqrt{2}\times2\sqrt{2})R45°-(2\times2)$ transition onto the Ising model as shown in Fig. 17. At low temperatures, the

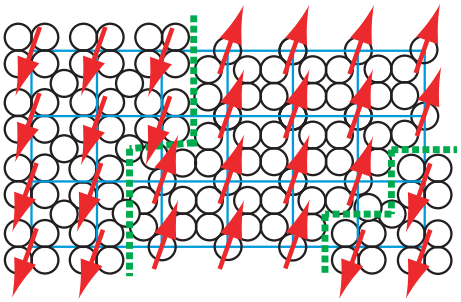

Fig. 17. A possible Ising-model representation of the order–disorder ($(2\sqrt{2} \times 2\sqrt{2})R45°$ – (2×2)) transition on In/Cu(001). Overlayed square lattice is for $(2\sqrt{2} \times 2\sqrt{2})R45°$. Broken lines indicate anti-phase boundary.

$(2\sqrt{2} \times 2\sqrt{2})R45°$ domain is well developed over the surface with a correlation length of > 1600 Å, corresponding to a "ferromagnetic" order. At $T = T_{cl}$, antiphase boundaries are created, which destroys the long-range order. Two types of domains separated by antiphase boundaries give rise to sharp (2×2) diffraction spots and diffuse $(2\sqrt{2} \times 2\sqrt{2})R45°$ spots. With increasing density of the antiphase boundary, diffuse $(2\sqrt{2} \times 2\sqrt{2})R45°$ spots are further broadened and weakened.

4.3 Mechanism of the phase transition

Now let us discuss the mechanism of the phase transition, which should explain both the results of ARPES and critical X-ray scattering.

First of all, it should be stated that the overall phenomena cannot be explained by the weak-coupling theory which predicts the BCS-like behavior for both the structural and electronic order parameter with the same T_c. The experiments show that the electronic gapped–degapped transition takes place at 60 K higher than the lattice transition. Interestingly, the Sn/Cu(001) also exhibits a gapped–degapped transition at ∼40 K higher than the structural transition, which may suggest that a common mechanism operates in the two cases.

We then should examine how the lattice and electrons behave at each temperature range. Let us start with the temperature range $T < T_{cl}$. In this temperature range, the long-range order is maintained with a lattice correlation length as long as ∼2000 Å. On the other hand, the lower-band maximum at the CDW gap is shifted upward by 50 meV, which corresponds to the decrease of the total CDW gap of ∼140 meV (16% of the total gap 860 meV), between 120 and 300 K. The lower-band maximum is further shifted by 30 meV between 300 and 345 K. The decrease of the band gap with increasing temperature may be induced by thermal lattice expansion, which decreases the gap by band

narrowing, and thermal vibration of the lattice [103]. These effect, however, seems to be not large enough to account for the observed shift. We should then consider the effect of thermal exciation of electrons into the upper band in a mechanism described below, which screens the electron–phonon coupling and hence decreases the CDW gap.

At $T > T_{cl}$, the band gap decreases steeply and goes to zero at $T_{ce} = 405$ K. The overall behavior of the gap is apparently in agreement with the mean-field theory, which suggests the substantial contribution of the surface electronic entropy. One may argue against this explanation that, because of the large CDW gap, 860±180 meV at $T = 0$, thermal excitation across the gap is negligible at temperatures studied. There, however, is an important point, peculiar to metal surfaces, that should be emphasized. The surface resonance band that forms the CDW gap in the low-temperature phase coexists in the same k space with the metallic bands of the bulk Cu (Fig. 18). As the wave functions of the surface resonance band penetrates well into the substrate, excitation of electrons from bulk states at $E_{\rm F}$ to the upper surface resonance band takes place easily. The energy separation of the upper-band minimum from $E_{\rm F}$ is small, δ_u =230±150 meV, at the k point of Fig. 13. While the total band gap 2Δ defines the condensation energy of CDW and determines the stability of the CDW ground state as in the CDW states in bulk materials, it is δ_u that governs the electronic entropy of the CDW states on metal surfaces.

The change in the electronic structure as described above should be associated with the displacive structural change. Crystal truncation rods (CTRs) measured at 25 and 455 K were mostly unchanged, which suggested that the local structure within a (2×2) unit cell is similar for low- and high-temperature phases [19]. However, CTRs showed a slight but reproducible change depending on the temperature, which may be due to the displacive structural change. Most recently, a grazing incidence X-ray diffraction experiment was carried out for the low-temperature $(2\sqrt{2} \times 2\sqrt{2})R45^\circ$ phase [104]. This indicates that the surface has a p2mm symmetry rather than a p4mm symmetry assumed in the previous works [71,72]. The quantitative structural analysis above T_{ce}, in particular, the examination of whether the surface maintains the p2mm distortion or transforms to p4mm, should be a key to solve the problem.

On the other hand, we should also examine the effect of the critical fluctuation on the energy gap, as the steep decrease of the gap takes place at temperature range corresponding to the enhanced critical fluctuation of the lattice order–disorder transition. Since the CDW gap is formed by the $(2\sqrt{2} \times 2\sqrt{2})R45^\circ$ lattice potential, the destruction of the $(2\sqrt{2} \times 2\sqrt{2})R45^\circ$ long-range order at $T = T_{cl}$ and the decrease of the lattice correlation length at $T > T_{cl}$ can, in principle, have an influence on the gap.

In order to discuss this effect semiquantitatively, we define the CDW corre-

lation length ξ_{CDW}. As shown in Figs. 11 and 13, the CDW energy gap is developed in a finite k-space width of $\delta k \approx 0.10$ Å^{-1} about the surface Brillouine zone boundary. Summing up the electron wavefunctions among this k interval would form a wavepacket of a size $\xi_{CDW} = 2\pi/\delta k \approx 60$ Å, which is defined as the CDW correlation length. [5] This does not necessarily mean that the surface is separated into patches of an average size of ξ_{CDW} in the CDW phase. In the ground state, the CDW "wavepackets" are coherently ordered to give rise to much longer lattice correlation length ξ_l.

The meaning of ξ_{CDW} is more clearly explained by stating that the formation of the CDW gap extending for δk in the k space requires that the lattice is coherently ordered in a length scale at least for ξ_{CDW}. It is therefore argued that, (1) when the lattice correlation length ξ_l is larger than ξ_{CDW}, the CDW gap is well developed, (2) when ξ_l decreases and becomes comparable to ξ_{CDW}, the spatial distribution of the CDW wavefunction starts to be limited by ξ_l rather than ξ_{CDW}, and (3) when $\xi_l < \xi_{CDW}$, the CDW gap should be decreased because of the destruction of CDW wavepackets. On the other hand, the decrease of the gap due to the shortening of ξ_l causes the increase of the electronic energy and entropy which corresponds to the displacive transition at a temperature much lower than anticipated by the mean-field description of the gap size.

The result of X-ray scattering (Fig.16) shows that ξ_l decreases from ∼1600 Å at $T = T_{cl}$ to ∼130 Å at $T = 380$ K, where the steep decrease of the CDW gap starts, and ∼80 Å at $T = T_{ce}$. While ξ_l is still larger than ξ_{CDW} at these temperatures, they are on the same order. This suggests that the lattice fluctuation effect may have some contribution to the decrease of the CDW gap. The ARPES spectrum at 374 K shown in Fig. 13(c) exhibits weak but significant photoemission intensity between the lower-band maximum and the upper-band minimum, which may be due to the contribution from patches with sizes smaller than the average at that temperature.

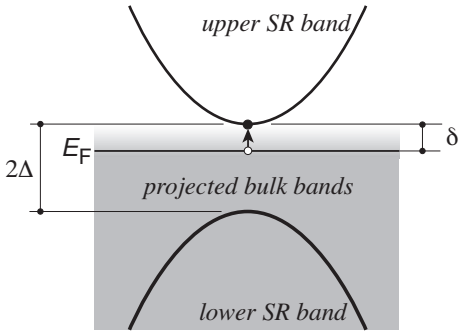

Fig. 18. Schematic of the surface resonance (SR) bands and bulk metallic bands. 2Δ denotes the CDW gap formed in the surface resonance bands, and δ denotes the energy separation of the upper-band minimum from $E_{\rm F}$.

5 Summary – Surface Peierls transition

The Peierls-type CDW transition on metal surfaces is different from that in bulk materials with low-dimensional electronic structure. While the CDW gap in the latter case is a true energy gap of the system, the "CDW gap" in the former case, i.e., the energy difference between the maximum of the lower surface-resonance band and the minimum of the upper surface-resonance band, does not represent the energy gap of the whole system (which is metallic and has no true energy gap across $E_{\rm F}$!). In the case of ideal low-dimensional systems, the stabilization energy of the CDW ground state as well as the electronic entropy of the metallic state are governed by the CDW energy gap. For the metal surface systems (Fig. 18), the ground-state stabilization energy is indeed determined by the CDW gap of the surface resonance bands but the electronic entropy is dominated by the energy difference between the upper band minimum and $E_{\rm F}$ of the whole system. This characteristics of the metal surface systems results in much lower T_{ce} than expected from the CDW gap.

We now have two typical examples of the surface Peierls transition on metals: One on surfaces of W(001) and Mo(001) as reviewed in section 2.4 and the other on Cu(001) covered with heavier p-block metallic elements. The CDW ground states have a CDW gap of $2\Delta \sim$2 eV in the former case and 0.5–1 eV in the latter case, indicating the large stabilization energy of these ground states as compared with the weak-coupling CDWs. The difference that separates these two cases from each other is, firstly, that of the energy separation between

[5] In ref.[19], the CDW correlation length was estimated by $\hbar v_{\rm F}/\pi\Delta$ [20,105], which has an essentially the same meaning as described above, to be ∼8 Å. This should be multiplied by 2π to be compared with the lattice correlation length ξ_l because of the difference in the unit of k in the nomenclature of X-ray diffraction and electronic structure theories. The correction due to electron effective mass requres that the value should be further multiplied by ∼1.3, which eventually results in $\xi_{CDW} = 60$ Å.

E_{F} and the upper CDW band minimum: $\delta_u \sim 1$ eV for W(001) [69] and $\delta_u \sim 0.2$ eV for In/Cu(001). The relatively small gap on Cu(001) suggests that the electronic excitation to the upper band is significant at around room temperature, which may induces weak-coupling-like displacive process. This can explain the shift of the lower-band maximum below 300 K on In/Cu(001) as well as the large difference of T_{ce}: > 1000 K for W(001) (see section 2.4) and ~ 400 K for In/Cu(001) and Sn/Cu(001).

The second, equally important factor that separates the two cases is the difference in the CDW correlation length ξ_{CDW}, which is estimated to be $\lesssim$7 Å for W(001)-$(\sqrt{2}\times\sqrt{2})R45°$ and ∼60 Å for Cu(001)-$(2\sqrt{2}\times 2\sqrt{2})R45°$-In. The difference in ξ_{CDW} reflects the character of the surface electronic states involved in the Fermi surface nesting. In the case of Cu(001) covered by In and Sn, it is a highly dispersed p band that forms the Fermi surface, while it is a much localized d band in the case of W(001) and Mo(001). While order–disorder transitions take place in both cases, it is only at very high temperature that the lattice correlation length ξ_l for W(001) becomes comparable with the very small ξ_{CDW}, thus making the conventional strong-coupling scenario a good description of the transition. On Cu(001) covered with In and Sn, because of the long CDW correlation length, the temperature at which $\xi_l \sim \xi_{CDW}$ is only a little (50–100 K) higher than the order–disorder transition temperature, which defines the upper limit of T_{ce}.

For a CDW system with long spacial coherence, the decrease of ξ_l due to the disordering with increasing temperature results in the degapping at a temperature corresponding to $\xi_l \sim \xi_{CDW}$, which then lowers the stabilization energy of the CDW state. It thus turns out that the disordering enhances the displacive process. In other word, the lattice entropy drives the electronic gapped–degapped process. This process is different in mechanism from that driven by electronic excitation across the gap. On Cu(001) covered with In and Sn, both the mechanism may be responsible to the gapped–degapped transition.

As a summary of this article, the author suggests that the CDW transitions are classified according to the gap size and the CDW correlation length (Fig. 19). For the case with a small gap and a long CDW correlation lenght (top left corner), the CDW stabilization energy is scaled to Δ^2 and a weak-coupling transition driven by electronic entropy is expected. The mean-field theory predicts for such a case a displacive transition in which the CDW gap and the lattice distortion change simultaneously. For the opposite case, i.e., that with a large gap and a short CDW correlation length (bottom right corner), the gap extends for a wide k region and hence the stabilization energy is scaled to Δ. The system is expected to behave according to the strong-coupling scenario: a lattice-entropy-driven order–disorder process takes place at a temperature much lower than that expected from the large gap for a weak-coupling tran-

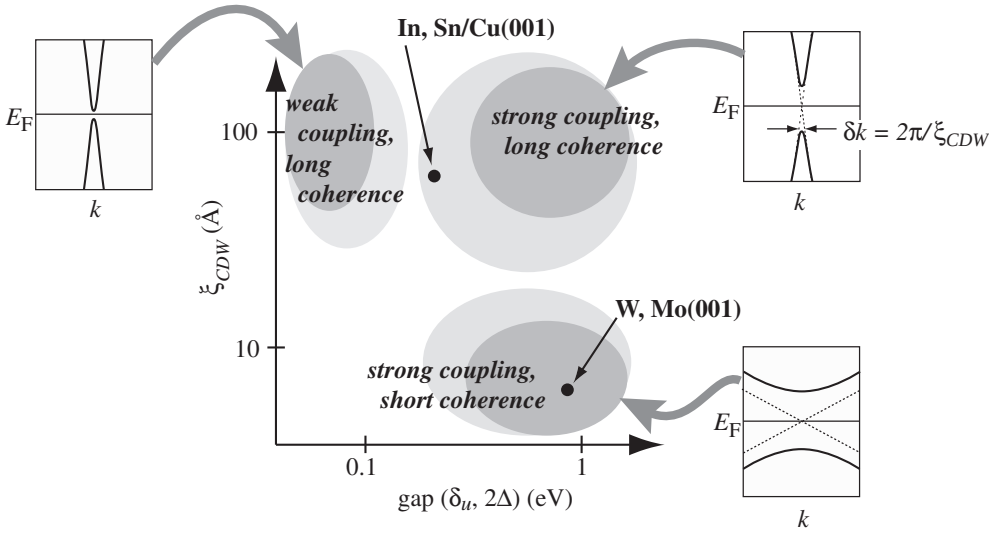

Fig. 19. Classification of the CDW transition according to the gap size, δ_u in the case of metal surfaces or 2Δ in the case of quasi-low-dimensional metals, and the CDW correlation length, ξ_{CDW}. One-dimensional band structure for each case is schematically shown.

sition, and the lattice distortion is maintained up to a very high temperature because of the short CDW correlation length (which means that the interaction is quite localized). The transition on W(001) and Mo(001) should be located here. In the case of a large gap and a long CDW correlation length (top right corner), the CDW stabilization energy is scaled to Δ^2 because the gap is restricted in a narrow k region. The CDW transition in this case proceeds in two steps as in the strong-coupling cases, but the displacive (gapped–degapped) process takes place at temperature only a little above that for the order–disorder transition. The displacive process in this case is driven predominantly by lattice entropy, while electronic entropy can contribute when the gap is relatively small.

The long CDW correlation length of the ground state on Cu(001) covered with In and Sn might have located the transition on this surface in the weak-coupling regime if the energy gap was a little smaller. In reality, the transition on this surface is classified into the third category. The relatively small value of δ_u suggests that electronic entropy contribute to the gapped–degapped transition as well.

Petersen et al. [5] suggested that the phase transition between $(\sqrt{3}\times\sqrt{3})R30°$ and (3×3) phases on α-Sn/Ge(111) can also be understood within the framework of the strong-coupling CDW scenario. In the low-temperature (3×3) phase, one Sn atom per unit cell is displaced upwards while the other two Sn atoms are displaced downwards. The band structure for the hypothetical in-plane $(\sqrt{3}\times\sqrt{3})R30°$ structure indicates that the surface bands are degenerated almost over the entire surface Brillouine zone when folded back into the

(3×3) surface Brillouine zone. The (3×3) structure is stabilized by Jahn-Teller-type rehybridization, resulting in one fully occupied surface band due to the more s-like dangling bond on the Sn atom displaced upwards and two metallic bands due to the dangling bond of the other two Sn atoms [5,6,106,107]. The comparison of the band structures for $(\sqrt{3} \times \sqrt{3})R30^\circ$ and (3×3) suggests that *the band due to the Sn atom displaced upwards is shifted uniformly by ∼0.2 eV to higher binding energy over the entire surface Brillouine zone.* This implies that the interaction involved is quite localized and does not necessarily need the k-space description. If one describes the system in terms of strong-coupling CDW, the "CDW correlation length" in this case is smaller than the unit cell size. This is in accordance with the fact that the transition at ∼220 K is an order–disorder one and the surface is disordered well above the transition temperature [8–10,108–110].

Acknoledgements

The author thanks Drs. Takeshi Nakagawa and Shinichiro Hatta, and Prof. Akio Yoshimori for enlightening discussions.

References

[1] J. M. Carpinelli, H. H. Weitering, E. W. Plummer, R. Stumpf, Nature 381 (1996) 398.

[2] J. M. Capinelli, H. H. Weitering, M. Bartkowiak, R. Stumpf, E. W. Plummer, Phys. Rev. Lett. 79 (1997) 2859.

[3] H. W. Yeom, S. Takeda, E. Rotenberg, I. Matsuda, K. Horikoshi, J. Schaefer, C. M. Lee, S. D. Kevan, T. Ohta, T. Nagao, S. Hasegawa, Phys. Rev. Lett. 82 (1999) 4898.

[4] T. Nakagawa, G. I. Boishin, H. Fujioka, H. W. Yeom, I. Matsuda, N. Takagi, M. Nishijima, T. Aruga, Phys. Rev. Lett. 86 (2001) 854.

[5] L. Petersen, Ismail, E. W. Plummer, Prog. Surf. Sci. 71 (2002) 1.

[6] J. Ortega, R. Pérez, F. Flores, J. Phys.: Condens. Matter 14 (2002) 5979.

[7] T. -C. Chiang, M. Y. Chou, T. Kidd, T. Miller, J. Phys.: Condens. Matter 14 (2002) R1.

[8] G. Le Lay, V. Yu. Aristov, O. Boström, J. M. Layet, M. C. Asenio, J. Avila, Y. Huttel, A. Cricenti, Appl. Surf. Sci. 123/124 (1998) 440.

[9] R. I. G. Uhrberg, T. Balasubramanian, Phys. Rev. Lett. 81 (1998) 2108.

[10] J. Avila, A. Mascaraque, E. G. Michel, M. C. Asensio, G. Le Lay, J. Ortega, R. Pérez, F. Flores, Phys. Rev. Lett. 82 (1999) 442.

[11] W. L. McMillan, Phys. Rev. B16 (1977) 643.

[12] E. Tosatti, in: A. Pekalski and J. Przystawa (Eds.), Modern Trends in the Theory of Condensed Matter, Springer-Verlag, Berlin, 1980, p. 501.

[13] E. Tosatti, in: E. Bertel and M. Donath (Eds.), Electronic Surface States and Interface States on Metallic Systems, World Scientific, Singapore, 1995, p. 67.

[14] T. Aruga, J. Phys. Condens. Matter 14 (2002) 8393.

[15] T. Nakagawa, H. Okuyama, M. Nishijima, T. Aruga, H. W. Yeom, E. Rotenberg, B. Krenzer, S. D. Kevan, Phys. Rev. B 67 (2003) 241401(R).

[16] T. Nakagawa, H. W. Yeom, E. Rotenberg, B. Krenzer, S. D. Kevan, H. Okuyama, T. Aruga, Phys. Rev. B 73 (2006) 075407.

[17] J. Martinez-Blanco, V. Joco, H. Ascolani, A. Tejeda, C. Quiros, G. Panaccione, T. Balasubramanian, P. Segovia, E. G. Michel, Phys. Rev. B 72 (2005) 041401.

[18] S. Hatta, H. Okuyama, M. Nishijima, T. Aruga, Phys. Rev. B 71 (2005) 041401(R).

[19] S. Hatta, H. Okuyama, T. Aruga, O. Sakata, Phys. Rev. B 72 (2005) 081406(R).

[20] G. Grünner, Density Waves in Solids, Addison Wesley, Reading, Massachusets, 1994.

[21] S. Kagoshima, H. Nagasawa, T. Sanbongi, One-Dimensional Conductors, Springer, Berlin, 1988.

[22] R. E. Peierls, Quantum Theory of Solids, Clarendon Press, Oxford, 1955.

[23] W. Kohn, Phys. Rev. Lett. 2 (1959) 393.

[24] R. Stedman, L. Almqvist, G. Nilsson, G. Raunio, Phys. Rev. 162 (1967) 545.

[25] B. Renker, H. Rietschel, L. Pintschovius, W. Glåser, P. Brüesch, D. Kuse, M. J. Rice, Phys. Rev. Lett. 30 (1973) 1144.

[26] R. Prasad, S. Auluck, S. K. Joshi, J. Phys. C: Solid State Phys. 8 (1975) L139.

[27] G. Shirane, S. M. Shapiro, R. Comès, A. S. Garito, A. J. Heeger, Phys. Rev. B 14 (1976) 2325.

[28] J. P. Pouget, S. M. Shapiro, G. Shirane, A. S. Garito, A. J. Heeger, Phys. Rev. B 19 (1979) 1792.

[29] J. R. Schrieffer, Theory of Superconductivity, Benjamin, New York, Amsterdam, 1964.

[30] G. Grüner, Rev. Mod. Phys. 60 (1988) 1129.

[31] K. Yonehara, L. D. Schmidt, Surf. Sci. 25 (1971) 238.

[32] T. E. Felter, R. A. Barker, P. J. Estrup, Phys. Rev. Lett. 38 (1977) 1138.

[33] M. K. Debe, D. A. King, J. Phys. C: Solid State Phys. 10 (1977) L303.

[34] E. Tosatti, Solid State Commun. 25 (1978) 637.

[35] J. E. Inglesfield, Prog. Surf. Sci. 20 (1985) 105.

[36] J. Jupille, D. A. King, in: D. A. King and D. P. Woodruff (Eds.), The Chemical Physics of Solid Surfaces vol. 7, Springer, Amsterdam, 1994, p. 35.

[37] M. K. Debe, D. A. King, Phys. Rev. Lett. 39 (1977) 708.

[38] M. K. Debe, D. A. King, Surf. Sci. 81 (1979) 193.

[39] J. A. Walker, M. K. Debe, D. A. King, Surf. Sci. 104 (1981) 405.

[40] J. B. Pendry, K. Heinz, W. Oed, H. Landskron, K. Müller, G. Schmidtlein, Surf. Sci. 193 (1988) L1.

[41] H. Landskron, N. Bickel, K. Heinz, G. Schmidtlein, K. Müller, J. Phys. Chem. 1 (1989) 1.

[42] G. Schmidt, H. Zagel, H. Landskron, K. Heinz, K. Müller, J. B. Pendry, Surf. Sci. 271 (1992) 416.

[43] M. S. Altman, P. J. Estrup, I. K. Robinson, Phys. Rev. B 38 (1988) 5211.

[44] J. Lee, D.-J. Huang, J. L. Erskine, Phys. Rev. B 51 (1995) 13824.

[45] J. Jupille, K. G. Purcell, D. A. King, Phys. Rev. B 39 (1989) 6871.

[46] E. Hulpke, D.-M. Smilgies, Phys. Rev. B 43 (1991) 1260.

[47] M. L. Hildner, R. S. Daley, T. E. Felter, P. J. Estrup, J. Vac. Sci. Technol. A 9 (1991) 1604.

[48] D.-M. Smilgies, P. J. Eng, I. K. Robinson, Phys. Rev. Lett. 70 (1993) 1291.

[49] R. S. Daley, T. E. Felter, M. L. Hildner, P. J. Estrup, Phys. Rev. Lett. 70 (1993) 1295.

[50] L. D. Roelofs, S. M. Foiles, Phys. Rev. B 48 (1993) 11287.

[51] I. K. Robinson, A. A. MacDowell, M. S. Altman, P. J. Estrup, K. Evans-Rutterrodt, J. D. Brock, R. J. Birgeneau, Phys. Rev. Lett. 62 (1989) 1294.

[52] T. E. Felter, J. Vac. Sci. Technol. A 2 (1984) 1008.

[53] B. Salanon, J. Lapujoulade, Surf. Sci. 173 (1986) L613.

[54] I. Stensgaard, K. G. Purcell, D. A. King, Phys. Rev. B 39 (1989) 897.

[55] K. Evans-Rutterrodt, R. J. Birgeneau, E. D. Specht, J. W. Chung, J. D. Brock, M. S. Altman, P. J. Estrup, I. K. Robinson, A. A. MacDowell, J. Vac. Sci. Technol. A 7 (1989) 2209.

[56] D. G. Kelly, R. F. Lin, M. A. Van Hove, G. A. Somorjai, Surf. Sci. 224 (1989) 97.

[57] M. L. Hildner, R. S. Daley, T. E. Felter, P. J. Estrup, Phys. Rev. B 52 (1995) 9050.

[58] H.-J. Ernst, E. Hulpke, J. P. Toennies, Phys. Rev. B 46 (1992) 16081.

[59] H.-J. Ernst, E. Hulpke, J. P. Toennies, Phys. Rev. Lett. 58 (1987) 1941.

[60] E. Hulpke, D.-M. Smilgies, Phys. Rev. B 40 (1989) 1338.

[61] E. Hulpke, D.-M. Smilgies, Phys. Rev. B 42 (1990) 9203.

[62] A. Fasolino, E. Tosatti, Phys. Rev. B 35 (1983) 4264.

[63] C. Z. Wang, A. Fasolino, E. Tosatti, Phys. Rev. Lett. 59 (1987) 1845.

[64] C. Z. Wang, A. Fasolino, E. Tosatti, Phys. Rev. B 37 (1988) 2116.

[65] W. K. Han, S. C. Ying, D. Sahu, Phys. Rev. B 41 (1990) 4403.

[66] W. K. Wang, S. -C. Ying, Phys. Rev. B 46 (1992) 1849.

[67] K. Terakura, I. Terakura, Y. Teraoka, Surf. Sci. 86 (1979) 535.

[68] I. Terakura, K. Terakura, N. Hamada, Surf. Sci. 111 (1981) 479.

[69] R. Yu, H. Krakauer, D. Singh, Phys. Rev. B 45 (1992) 8671.

[70] T. Nakagawa, S. Mitsushima, H. Okuyama, M. Nishijima, T. Aruga, Phys. Rev. B 66 (2002) 085402.

[71] K. Pussi, T. McEvoy, C. J. Barnes, A. A. Cafolla, E. AlShamalleh, M. Lindroos, Surf. Sci. 526 (2003) 141.

[72] S. Hatta, C. J. Walker, O. Sakata, H. Okuyama, T. Aruga, Surf. Sci. 565 (2004) 144.

[73] C. Argile, G. E. Rhead, Thin Solid Films 87 (1982) 265.

[74] E. McLoughlin, A. A. Cafolla, E. AlShamaileh, C. J. Barnes, Surf. Sci. 482-485 (2001) 1431.

[75] K. Pussi, E. AlShamaileh, E. McLoughlin, A. A. Cafolla, M. Lindroos, Surf. Sci. 549 (2004) 24.

[76] F. Abel, C. Cohen, J. A. Davies, J. Moulin, D. Schmaus, Appl. Surf. Sci. 44 (1990) 17.

[77] C. Binns, C. Norris, Surf. Sci. 115 (1982) 395-416.

[78] C. Binns, M. G. Barthelslabrousse, C. Norris, J. Phys. C **17** (1984) 1465-1473.

[79] C. Binns, C. Norris J. Phys.: Condens. Matt. 3 (1991) 5425-5436.

[80] C. Binns, C. Norris, M. G. Barthelslabrousse, Phys. Scripta T45 (1992) 283.

[81] J. Henrion, G. E. Rhead, Surf. Sci. 29 (1972) 20.

[82] A. Sepulsiva, G. E. Rhead, Surf. Sci. 66 (1977) 436.

[83] C. Argile, G. E. Rhead, Surf. Sci. 78 (1978) 115.

[84] C. Argile, G. E. Rhead, Surf. Sci. 78 (1978) 125.

[85] F. Delamare, G. E. Rhead, Surf. Sci. 35 (1972) 172.

[86] H. L. Meyerheim, M. De Santis, W. Moritz, I. K. Robinson, Surf. Sci. 418 (1998) 295.

[87] S. Hatta, H. Okuyama, M. Nishijima, T. Aruga, Appl. Surf. Sci. 237 (2004) 270.

[88] X. Gao, Y. M. Zhou, S. C. Wu, D. S. Wang, Phys. Rev. B 66 (2002) 073405.

[89] T. Kennedy, E. H. Lieb, Phys. Rev. Lett. 59 (1987) 1309.

[90] P. Blaha, K. Schwarz, G. K. H. Madsen, K. Kvasnicka, J. Luitz, WIEN2k, An Augmented Plane Wave + Local Orbital Program for Calculating Crystal Properties, Technical Universitat Wien, Wien, Austria, 2001.

[91] J. A. Appelbaum, G. A. Baraff, D. R. Hamann, Phys. Rev. B14 (1976) 1623.

[92] W. A. Harrison, J. Vac. Sci. Technol. 16 (1979) 1492.

[93] F. Bechstedt, Principles of Surface Physics, Springer-Verlag, Berlin, Heidelberg, 2003.

[94] G. -H. Gweon, J. D. Denlinger, J. A. Clack, J. W. Allen, C. G. Olson, E. D. DiMasi, M. C. Aronson, B. Foran, S. Lee, Phys. Rev. Lett. 81 (1998) 886.

[95] F. Zwick, D. Jérome, G. Margaritondo, M. Onellion, J. Voigt, M. Grioni, Phys. Rev. Lett. 81 (1998) 2974.

[96] R. Liu, W. C. Tonjes, V. A. Greenya, C. G. Olson, R. F. Frindt, Phys. Rev. B 61 (2000) 5212.

[97] C. R. Ast, H. Hochst, Phys. Rev. Lett. 90 (2003) 016403.

[98] J. R. Ahn, H. W. Yeom, H. S. Yoon, I. -W. Lyo, Phys. Rev. Lett. 91 (2003) 196403.

[99] O. Sakata, Y. Furukawa, S. Goto, T. Mochizuki, T. Uruga, T. Takeshita, T. Ohashi, T. Matsushita, S. Takahashi, Surf. Rev. Lett. 10 (2003) 543.

[100] J. Ihm, D. H. Lee, J. D. Joannnopoulos, J. J. Xiong, Phys. Rev. Lett. 51 (1983) 1872.

[101] T. Tabata, T. Aruga, Y. Murata, Surf. Sci. 179 (1987) L63.

[102] M. Kubota, Y. Murata, Phys. Rev. B 49 (1994) 4810.

[103] N. W. Ashcroft, N. D. Mermin, Solid State Physics, Harcourt, 1976.

[104] S. Hatta, O. Sakata, H. Okuyama, T. Aruga, to be published.

[105] M. Tinkham, Introduction to Superconductivity, McGraw-Hill, New York, 1975.

[106] S. de Gironcoli, S. Scandolo, G. Balabio, G. Santoro, E. Tosatti, Surf. Sci. 454-456 (2000) 172.

[107] R. Pérez, J. Ortega, F. Flores, Phys. Rev. Lett. 86 (2001) 4891.

[108] L. Floreano, D. Cvetko, G. Bavdek, M. Benes, A. Morgante, Phys. Rev. B 64 (2001) 075405.

[109] L. Petaccia, L. Floreano, A. Goldoni, D. Cvetko, A. Morgante, L. Grill, A. Verdini, G. Comelli, G. Paolucci, S. Modesti, Phys. Rev. B 64 (2001) 193410.

[110] F. Ronci, S. Colonna, S. D. Thorpe, A. Cricenti, G. Le Lay, Phys. Rev. Lett. 95 (2005) 156101.